Water-Promoted C-C Coupling Reaction in Plasma-catalytic CO_2 Hydrogenation for Ethanol Production

Shengyan Meng[1†], Zhaolun Cui[2,6†], Qian Chen[1†], Hang Zhang[3], Shangkun Li[4], Erik Cornelis Neyts[4], Evgenii Vlasov[5], Kellie Jenkinson[5], Sara Bals[5], Dezheng Yang[2], Min Liu[3,*], Yi Liu[1,*], Annemie Bogaerts[4], An-Hui Lu[1,*] and Yanhui Yi[1,*]

[1]State Key Laboratory of Fine Chemicals, School of Chemical Engineering, Dalian University of Technology, Dalian 116024, China;
[2]Key Lab of Materials Modification by Laser, Ion, and Electron Beams, Dalian University of Technology, Dalian 116024, China;
[3]State Key Laboratory of Powder Metallurgy, School of Physics, Central South University, Changsha 410083, China;
[4]Research group PLASMANT, Department of Chemistry, University of Antwerp, Universiteitsplein 1, BE-2610 Wilrijk-Antwerp, Belgium;
[5]Electron Microscopy for Materials Science (EMAT), University of Antwerp, Universiteitsplein 1, BE-2610 Wilrijk-Antwerp, Belgium;
[6]School of Electric Power Engineering, South China University of Technology, Guangzhou 510630, China;

[†]Equally contributed to this work.

ABSTRACT

The conversion of CO_2 into alcohols has attracted widespread interest. Herein, we present an approach for the plasma-catalytic CO_2 hydrogenation to ethanol over a Cu_2O/CeO_2 catalyst under atmospheric pressure at a low temperature of ~75 °C. The Cu_2O/CeO_2 catalyst initially exhibits low ethanol selectivity (2.1%), which dramatically increases to 56% (78% total alcohols selectivity) with the assistance of water. D_2O and $H_2{}^{18}O$ isotope-tracing experiments reveal the partial decomposition of water and the active involvement of its derivatives in the multi-step pathway for ethanol synthesis. The multiple roles of H_2O in switching the alcohols production from methanol to ethanol are investigated. The plasma-generated OH in both adsorbed and radical states promote the C-C coupling via CO-H_2CO bonding and facilitates the hydrogenation through proton transfer. Additionally, the presence of adsorbed H_2O and OH enhances the desorption of ethanol, further enhancing alcohols selectivity. It is envisaged that these findings would bring inspirations for value-added transformation of CO_2 to produce higher alcohols and pave the way for efficient chemical processes.

Keywords: CO_2 hydrogenation, plasma catalysis, C_2H_5OH synthesis, C-C coupling, water-assisted catalysis, copper-based catalysts, DFT calculations

1. INTRODUCTION

As a major greenhouse gas, carbon dioxide (CO_2) holds the potential to serve as an abundant, cheap and renewable carbon source. Carbon capture and utilization (CCU) technology plays a pivotal role in converting CO_2 into high value-added chemicals, thereby contributing to the development of a sustainable low-carbon economy.[1] At present, significant advancements have been achieved in the conversion of CO_2 to carbon monoxide (CO), alcohols, olefins, and aromatics.[2-6] Among the alcohols products, ethanol (C_2H_5OH) has a higher energy density than methanol (CH_3OH) and has been widely used as a disinfectant, solvent and renewable fuel additive.[7]

However, the hydrogenation of CO_2 to C_2H_5OH remains a formidable challenge due to the thermodynamic stability of CO_2 and the intricacies involved in controlling C-C coupling reactions. Initially, Rh-based catalyst, as pioneered by Tanabe's group, demonstrated promise in this direction.[8] Besides the typical Rh-based catalysts, other noble metal catalysts (Au-,[9] Pt-,[10] Pd-based [11]) have been explored for CO_2 hydrogenation to C_2H_5OH. In recent years, non-noble metal and transition metal carbide catalysts have garnered significant attention as alternatives for CO_2 hydrogenation to C_2H_5OH, in which Cu- and Co-based catalysts have been shown effective on C_2H_5OH yields in thermal catalysis.[12-16] Nevertheless, as summarized in Table S1, most reported catalysts evaluated in fixed-bed reactors have struggled with poor C_2H_5OH selectivity.

In thermal catalysis, CO_2 hydrogenation for C_2H_5OH production can be improved by adding water (H_2O) to the feedstock. H_2O and its dissociation products are found to play a paramount role in C-C coupling and generation of alcohols.[10, 17-21] He et al. reported the water-promoted higher alcohols (C_2-C_4) generation at 200 ºC over a Pt/Co_3O_4 catalyst, achieving an ethanol selectivity of 17.3%.[10] They presumed that the water could facilitate the dissociation of CH_3OH into CH_3* (* means the adsorbed state), leading to C-C coupling through the CO*-CH_3* mechanism. Graciani et al. evaluated the multiple roles of H_2O on CO_2 conversion to ethanol over a $Pt/CeO_x/TiO_2(110)$ catalyst, showing an optimal ethanol selectivity of 38% at 280 ºC and 5 bar.[19] Water was found to promote the first hydrogenation step and enhance the surface coverage of C-containing species, which facilitate the C-C bond formation via CH_3*-H_2CO* coupling. As is clear from these examples, the C_2H_5OH synthesis in thermal catalysis often requires relatively high temperature and pressures, hindering its applications at milder conditions.

In contrast, plasma catalysis is gaining increasing interest, as it enables thermodynamically unfavorable reactions to proceed near room temperature and at atmospheric pressure.[22] Especially the non-equilibrium species and discharge effects reduce the activation barriers for rate-limiting steps and break the scaling relations, providing an attractive alternative for CO_2 conversion.[23] Currently, plasma-catalytic CO_2 hydrogenation has been investigated focusing on the production of C1 molecules (CO, CH_4 and CH_3OH).[24,25] Plasma-generated reactive species have been demonstrated to play a significant role in guiding the surface catalytic reactions via unique effects, including surface modification, pre-adsorption and

Eley-Rideal (E-R) reactions.[20,26,27] In this regard, combining with inspiration from He et al. that H_2O molecules promote C-C coupling reaction for C_2H_5OH production,[10] we may speculate that plasma-activated H_2O could have multiple roles in guiding the CO_2 hydrogenation to C_2H_5OH at mild conditions.

Herein, we report a novel plasma catalysis approach, achieving C_2H_5OH synthesis from CO_2 hydrogenation over a cost-effective Cu_2O/CeO_2 catalyst with the assistance of water at atmospheric pressure and ca. 75 °C (Figure S1 provides the temperature distribution measured by an infrared camera), showing ca. 56% C_2H_5OH selectivity and a total alcohols (methanol and ethanol) selectivity of around 78%. Furthermore, combination of isotope-tracing experiments and Density Functional Theory (DFT) calculations reveal the distinct C-C coupling reaction mechanism for C_2H_5OH production switched by H_2O, which is quite different from the mechanism previously reported. In the plasma, H_2O molecule is dissociated to produce adsorbed OH* species and gas phase OH radicals. The adsorbed OH* species is identified as a crucial factor in facilitating the C-C coupling reaction and hydrogenation for C_2H_5OH formation and its subsequent desorption over the Cu^+ catalyst. The gas phase OH radicals promote the hydrogenation and facilitate the OH* surface coverage. In this regard, the unique roles of water in plasma enable the stable C_2H_5OH yield with a high selectivity, which offers new opportunity for the higher alcohols production from CO_2.

2. METHODS

2.1 Catalyst preparation. $Cu(NO_3)_2 \cdot 5H_2O$ (99%, Tianjin Guangfu Technology Development Co., Ltd, China), oxide support materials (Shanghai Buwei Applied Materials Technology Co., Ltd, China). Deionized (DI) water was homemade.

Copper-based catalysts with various supports were prepared via incipient wetness impregnation, utilizing commercially available supports (Al_2O_3, SiO_2, Fe_2O_3, CeO_2, TiO_2, ZrO_2) as supporting materials, and subsequently calcined at 540 °C prior to use. Initially, the precursor salt $Cu(NO_3)_2 \cdot 5H_2O$ was dissolved in DI, and then the support was added to the solution and stirred for 15 minutes. A fixed Cu loading of 5 wt.% was achieved by adjusting the amount of precursor salt accordingly (XRF results indicate an actual loading of approximately 5.5 wt.%). Subsequently, the mixture was aged at room temperature for 12 hours and then overnight dried at 120 ºC in air. Following this, the samples underwent calcination in air for 5 hours in a muffle furnace at 800 ºC and were finally crushed and sieved into granules (20-40 mesh). To investigate the physicochemical properties of the catalysts, both fresh and spent catalysts were characterized by various methods. The fresh catalyst is denoted as Cat-F, while the collected spent catalyst is denoted as Cat-S (x-1), with x representing the content of H_2O based on CO_2.

2.2 Catalytic test. The schematic diagram of the experimental equipment is shown in Scheme S1. A coaxial dielectric barrier discharge (DBD) reactor with a water electrode was used to generate CO_2/H_2 plasma. A stainless-steel tube (2 mm outer diameter) was placed in the center of a DBD reactor, consisting of a pair of coaxial quartz cylinders (inner and outer quartz tubes) as high-pressure electrodes. The temperature of the circulating water (grounded electrode) was maintained at 60 °C, the discharge length was 60 mm, and the 4 mm discharge gap was completely packed by catalyst granules (20-40 mesh, ca. 2.2 g Cu_2O/CeO_2 catalyst). The input power was maintained at around 23 W, and the discharge frequency was fixed at 9.5 kHz. The individual reaction duration ranged from 3 to 5 hours, depending on the addition of water content.

CO_2 (98%, 18 mL/min) and H_2 (99.99%, 54 mL/min) were monitored using mass flow controllers and homogeneously mixed with water vapor generated by a steam generator at 110 °C before passing through the plasma reactor. The use of heating tape ensured complete encapsulation of the reactor by the gas before contact with the catalyst, thus guaranteeing the vaporized state of water. In this study, the maximum flow rate of gaseous water was 36 mL/min while the liquid water flow rate at the pump was 28.93 μL/min. It should be mentioned that the plasma discharge is influenced when the H_2O/CO_2 molar ratio exceeds 2 due to the electronegativity of H_2O. The liquid product was collected by a collector (mixture of isopropanol and liquid nitrogen below -120 °C) at the exhaust of the DBD reactor, and the decrease of the gas flow rate was measured by a soap-film flow meter. The distance between the exhaust pipe and the soap bubble flow meter was 3 meters, with a 6 mm inner diameter silicone tube, to mitigate the impact of product condensation on gas velocity. The composition of the exhaust gas was analyzed online by gas chromatography (Tianmei 7890 II equipped with a thermal conductivity detector and a TDX-01 chromatograph column, with H_2 as the carrier gas. The flame ionization detector used a TM-Al_2O_3/S column with N_2 as carrier gas) with the addition of 2% N_2 as an internal standard. The gas chromatography method samples every 15 minutes (with the exhaust gases being detected 2 hours later), and the final result is determined through the calculation of the average value (totaling approximately 8 results). Liquid products were analyzed by gas chromatography (Shimadzu GC-2014C, equipped with a flame ionization detector and a PEG-20M column) and GC-MS (Agilent 5975C, DB-1701 column). The mass spectrometry (MS) signal intensity of the exhaust gas was in-situ measured by a mass spectrometer (PFEIFFER, OmniStar) using SEM scanning mode. Considering the initial stage of the reaction, partial reduction of Cu species will cause weak fluctuations in the MS signal, and the sample used for MS analysis is the spent catalyst.

2.3 Catalyst characterization. The crystal structure of the catalyst was determined using an powder X-ray diffractometer (Rigaku, D-max 2400) with CuKα radiation. The measurement was operated in the range of 10-80° with a scanning rate of 5°/min at 50 mA and 240 kV. The texture information of the samples was measured by N_2 physisorption (Micromeritics ASAP 3020) at -196 °C. Before the measurement, the samples (0.2 g) were degassed at 350 °C for 5 hours. The surface area was determined based on the Brunauer-Emmett-Teller (BET) method, and the pore volume of the samples was calculated by t-plot method at a P/P_0 of 0.99. High-angle annular dark-field scanning transmission electron microscopy (HAADF-STEM) images of the catalysts were obtained using a “cubed” Thermo Fisher Scientific X-Ant-EM electron microscope operated at 300 kV. Energy-dispersive X-ray spectroscopy (EDX) mapping was used to retrieve an elemental distribution over the sample surface. The reduction properties of the catalysts were measured on a ChemBET Pulsar (Quanta chrome) chemical adsorption instrument. The samples (0.5 g) were purged for 1 hour at 450 °C under He atmosphere. After cooling to room temperature, the samples were heated to 500 °C at a rate of 10 °C/min in an Ar-H_2 atmosphere (120 mL/min, 10% H_2), and a TCD was used to detect the hydrogen consumption. X-ray photoelectron spectroscopy (XPS) was carried out on an ESCALAB 250Xi instrument (ThermoVG) with an AlKα X-ray source. The binding energy value of C1s (284.8 eV) was taken as a reference level to obtain chemical information of the elements on the catalyst surface. The Ar+ etching was carried out under the conditions of 2 kV by bombarding the catalyst surface. In this study, SiO_2 was chosen as the standard sample, with an etching rate set at approximately 10 nm/min. Hence, 60 s etching time resulted in an etch depth of approximately 10 nm on the catalyst surface. All catalysts were sealed in vacuum bags prior to characterization tests.

2.4 Plasma diagnostics. The electrical behavior was characterized by three indicators: discharge voltage (kV), discharge current (mA) and discharge frequency (kHz), which were detected by a digital oscilloscope (Tektronix, DPO 3012) with a high voltage probe and a current probe. In plasma systems, the Lissajous plots represent the charge in the plasma as function of voltage, and the enclosed area denotes the average power consumed by the discharge, i.e., the product of energy consumed per cycle and the frequency of the cycle. Furthermore, we used an in-situ Princeton Instruments ICCD emission spectrometer (SP 2758) with a 300 g/mm grating to diagnose the optical behavior in the CO_2/H_2 plasma. The slit width of the spectrometer was fixed at 20 μm and the exposure time was fixed at 2 s.

2.5 DFT calculation. All DFT calculations were performed in CP2K 7.0 package with the Quickstep module.[28,29] The molecular optimized (MOLOPT) and double-ζ valence plus polarization basis set was chosen combined with an auxiliary plane wave basis set with 600 Ry cutoff.[30] The Goedecker-Teter-Hutter pseudopotential (GTH) was applied for core-valence interactions.[31] The exchange and correlation effects were treated by Perdew-Burke-Ernzerhof (PBE) functional with spin unrestricted. Dispersion interactions were accounted for using Grimme's D3 approximation, together with Becke-Johnson damping.[32,33] The sampling of the Brillouin zone was limited to the Γ-point only.[34] The Broyden-Fletcher-Goldfarb-Shanno (BFGS) scheme was applied for geometry optimization. The location of the transition state (TS) was determined using the climbing image nudged elastic band (CI-NEB) method.[35] Vibration analysis was used to ensure that there was only one imaginary frequency at each transition state. A six-layer slab of $Cu_2O(111)$ was chosen to represent the surface.[36] It was modeled as a 2×2 super unit, containing 128 atoms. The bottom three layers were fixed throughout the calculations. The size of the simulated box was $10.458\times12.067\times40.000$ Å^3 with periodic boundaries along {X,Y,Z} directions. The adsorption energy E_{ad} was calculated as $E_{ad} = E_{system} - (E_{cat} + E_{gas})$, where E_{cat}, E_{gas} and E_{system} correspond to the internal energy at 0 K of the catalyst slab, gas phase molecule or atom and the adsorption system at their ground states. A positive value means that the adsorption process is endothermic. The top sites over unsaturated and saturated surface Cu atoms and O atoms are selected for adsorption tests. At each site, adsorbates in different orientations towards the catalyst surface are calculated and the stable one with higher E_{ad} are finally recorded. Elementary reactions considered in this study are selected according to the results of catalysts surface characterization, isotope-tracing experiments and reported studies with Cu-based catalysts or using similar catalyst structures.[11]

3. RESULTS AND DISCUSSION

3.1 Catalytic Performance. Based on controlled experiments, i.e., investigation of Cu-based catalysts (Figure S2) and reaction conditions (Figures S3-4) in CO_2 hydrogenation, we found that the Cu_2O/CeO_2 catalyst was capable of driving CO_2 hydrogenation to produce not only CH_3OH but also C_2H_5OH with relatively higher selectivity. Details of materials and methods are shown in Supporting Information. We systematically investigated the performance of the Cu_2O/CeO_2 catalyst in plasma-assisted CO_2 hydrogenation to produce C_2H_5OH with the addition of H_2O.

Figures 1 (a, b and c) show the effect of water content on product distribution, CO_2 conversion and energy consumption for the production of C_2H_5OH and CH_3OH over a Cu_2O/CeO_2 catalyst. With increasing H_2O content, the C_2H_5OH selectivity dramatically increases from 2.1% to 55.7%, while the CH_3OH selectivity first slightly increases and then gradually decreases (Figure 1a). The CO_2 conversion shows a trend similar to the CH_3OH selectivity (Figure 1b). Hence, the addition of a low content of water (H_2O/CO_2 molar ratio below 0.5) favors CH_3OH formation and CO_2 conversion, which is consistent with earlier reports [17,18] and our previous results [20]. A higher content of water promotes the selectivity of C_2H_5OH. However, under this condition (molar ratio of $H_2O/CO_2 = 2/1$), the CO_2 conversion decreases by one-third. This reduction may be caused not only by the lower discharge voltages (Figure S5), but also by the electron affinity of water, capturing electrons, which reduces the electron density in the plasma. Consequently, the rate of electron impact reactions decreases, slowing CO_2 dissociation. We have summarized the production rates of different products under various reaction conditions in Table S2. Figures S6-8 illustrate the gas chromatographic data, carbon balance and catalyst stability testing. It should be noted that we also observe the promotion of C_2H_5OH formation by water on Cu_2O/Al_2O_3, Cu_2O/SiO_2 and Cu_2O/Fe_2O_3 catalysts (Figure S9). As shown in Figures 1b and S9, there is clearly a trade-off between high C_2H_5OH selectivity at low CO_2 conversion upon more water addition, vs. low C_2H_5OH selectivity at high CO_2 conversion with lower water content.

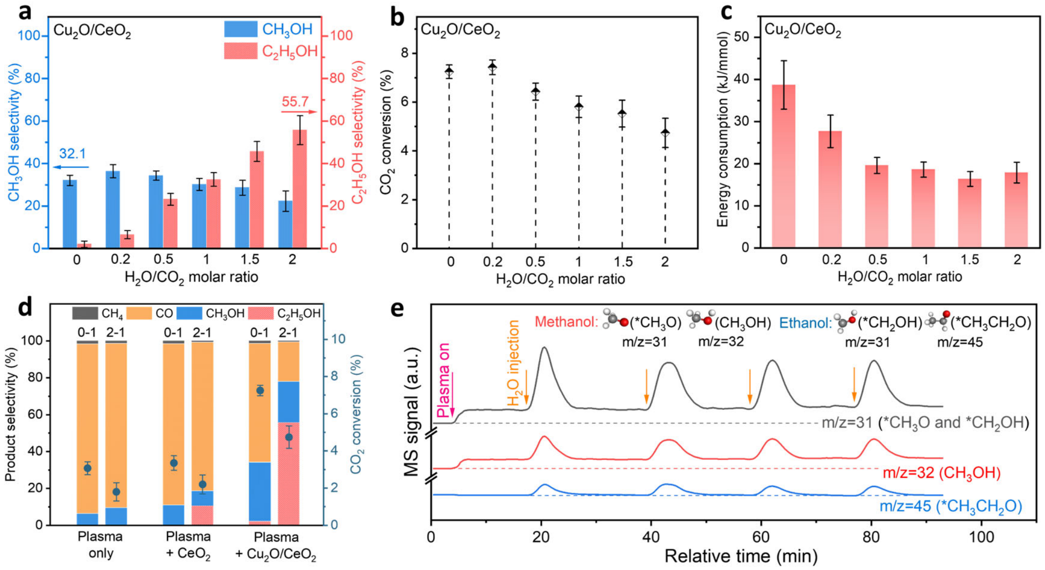

Figure 1. (a-c) Influence of H_2O/CO_2 molar ratio on (a) product selectivity, (b) CO_2 conversion and (c) energy consumption for C_2H_5OH and CH_3OH production over a 5 wt.% Cu_2O/CeO_2 catalyst (2.2 g); (d) Influence of reaction system and presence/absence of H_2O on product selectivity and CO_2 conversion (0-1 and 2-1 represent the H_2O/CO_2 molar ratio); (e) Temporal profiles of MS signals with different m/z values (corresponding to different species) in CO_2 hydrogenation through plasma catalysis over 5 wt.% Cu_2O/CeO_2 catalyst (2.2 g, pre-reduced catalyst) with intermittent addition of H_2O for 3 minutes of each injection (molar ratio of H_2O/CO_2 = 2/1). (Reaction conditions: 5 wt.% Cu loading, CO_2/H_2 = 1/3, input power 23 W, discharge frequency 9.5 kHz, 75 ºC, 1 atm pressure; error bars represent the standard deviation from at least three independent measurements).

Overall, the selectivity towards alcohols (CH_3OH and C_2H_5OH) substantially improves by the presence of H_2O molecules on the Cu_2O/CeO_2 catalyst, and 78.0% alcohols selectivity (22.3% CH_3OH and 55.7% C_2H_5OH) is achieved in the case of H_2O/CO_2 = 2/1. The energy consumption for alcohols formation also drops upon water addition in case of the Cu_2O/CeO_2 catalyst (Figure 1c), and the lowest energy consumption reaches 16.4 kJ/mmol for the H_2O/CO_2 molar ratio of 1.5. The CO selectivity from CO_2 hydrogenation at various water contents on Cu-based catalysts with different supports is shown in Figure S10, and the Cu_2O/CeO_2 catalyst displays the lowest CO selectivity of all catalysts. In addition, control experiments indicate that the Cu_2O/CeO_2 catalyst cannot activate CO_2 via H_2O in the absence of H_2. (Figure S11). Similar investigations carried out under both plasma and non-plasma conditions, as depicted in Figure S12, demonstrate that CO_2 cannot be converted at 75 °C and atmospheric pressure without the assistance of plasma. This underscores the crucial role of plasma and hydrogen in inducing catalytic reactions.

Figure 1d compares the product selectivity and CO_2 conversion for plasma only, plasma + CeO_2, and plasma + Cu_2O/CeO_2 catalyst with and without H_2O addition (0-1 and 2-1 denote the H_2O/CO_2 molar ratio), and Figure S13 shows the corresponding energy consumption for alcohols production. In the absence of catalysts (plasma only), C_2H_5OH is not observed in the products, which indicates that the C-C coupling reaction cannot be triggered in H_2/CO_2 plasma without the assistance of catalysts, regardless of H_2O. After packing the plasma with CeO_2 support (plasma + CeO_2), there is a slight increase in CO_2 conversion, but the combination of CeO_2 packing and H_2O addition leads to a clear C_2H_5OH production (10.5% selectivity). More interestingly, in the case of packing the plasma with Cu_2O/CeO_2 catalyst (plasma + Cu_2O/CeO_2), the coupling of Cu_2O/CeO_2 packing and H_2O addition results in a dramatic enhancement of the C_2H_5OH selectivity (55.7%), which suggests a clear synergy between plasma, Cu_2O/CeO_2 catalyst and H_2O molecules in promoting the C-C coupling reaction for C_2H_5OH production from CO_2 hydrogenation.

Figure 1e shows the temporal profiles of mass spectrometry (MS) signals with different m/z values in CO_2 hydrogenation through plasma catalysis over Cu_2O/CeO_2 catalyst with intermittent addition of H_2O (molar ratio of H_2O/CO_2 = 2/1). In the initial stage, i.e., after plasma on but before H_2O injection, the intensities of m/z = 31 (CH_3O and CH_2OH) and m/z = 32 (CH_3OH) both show an increase, indicative of the production of CH_3OH. The signal fluctuations observed at m/z = 45 (CH_3CH_2O) can be deemed negligible, owing to the low selectivity of C_2H_5OH. It should be noted that the catalyst was pre-reduced for the experiments, which explains why there is initially no increase for the signal value. Following each water injection, a sharp increase in m/z = 31, 32 and 45 suggests additional CH_3OH and C_2H_5OH generation, enhancing the alcohols synthesis (m/z = 31 is the primary signal for C_2H_5OH, indicative of fragmentation, while m/z = 45 represents a secondary signal). After each termination of H_2O injection, the intensity at m/z = 45 (CH_3CH_2O) nearly reverts to its initial level, suggesting minimal C_2H_5OH production in the CO_2/H_2 plasma when H_2O was not added. Furthermore, considering the prediction of Lustemberg et al. that water may occupy adsorption sites intended for CH_3OH on the catalyst surface,[37] thereby promoting its desorption, we speculate that water, beyond its role in C-C coupling reactions, might also influence the desorption of C_2H_5OH, as detailed in the DFT calculation section.

3.2 Diagnostics of the $CO_2/H_2(/H_2O)$ plasma. Figure 2a compares the waveforms of the discharge current of plasma-only and plasma packed with Cu_2O/CeO_2 catalyst. The Cu_2O/CeO_2 packing exhibits a somewhat higher intensity of discharge current compared with the plasma-only condition. Figure 2b shows the Lissajous plots corresponding to discharges of non-packed plasma and plasma packed with Cu_2O/CeO_2 catalyst. The shape of the Lissajous plots changes from a parallelogram (no packing) to an oval shape (packed with Cu_2O/CeO_2 catalysts), which is attributed to the increase in equivalent capacitance of the system with the addition of different materials.[38] Obviously, the slope of the discharge part in the plasma packing system is larger than in the non-packed system, corresponding to more discharge filaments, as also observed in (a), with a higher discharge efficiency ($P_{\text{plasma only}}$ = 9.3 W, $P_{\text{plasma + Cu2O/CeO2}}$ = 13 W, for the same input power of 23 W). Filamentary discharges are commonly beneficial for the electron density, and a higher intensity of the discharge current leads to a higher density of energetic electrons in the discharge area, which increases the possibility for activation, dissociation and ionization of the feedstock gases through inelastic collisions with energetic electrons.

We calculated the mean electron energy and the electron energy distribution function (EEDF) for the CO_2/H_2 plasma with and without H_2O) via Bolsig+, following a method proposed by Mei et al.[39,40] The mean electron energy is plotted as a function of the reduced electric field (E/N, i.e., ratio of electric field over gas number density, expressed in Td, where 1 Td = 10^{-21} V m²) in Figure 2c. The E/N, and thus the mean electron energy, of the packed plasma (by CeO_2 or Cu_2O/CeO_2) is much higher than that of plasma-only (no packing), mainly owing to the reduction in gas phase volume in case of the packing, causing the potential drop over a shorter distance, and thus a stronger electric field as well as electric field enhancement due to packing polarization.[41] Besides, EEDFs in Figure S14 demonstrate that there are more electrons with higher energy in the packed plasmas. H_2O addition slightly increases the fraction of high-energy electrons. In this regard, more reactive species are generated in the packed plasma upon electron impact dissociation, excitation and ionization of the feedstock molecules, enabling more significant reactions in the gas phase and at the catalyst surface.[40]

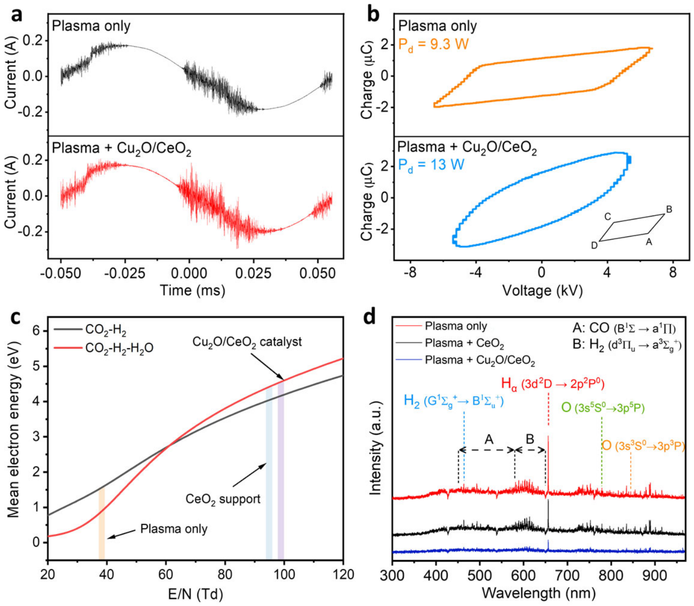

Figure 2. Results of plasma diagnostics. (a) Waveforms of discharge current, and (b) Lissajous plots (AB and CD segments are the discharge-on phases, and the catalyst packing leads to an increase in their slopes) for plasma-only and plasma + Cu_2O/CeO_2 catalyst; (c) Calculated mean electron energy as a function of reduced electric field (E/N; see text) for CO_2/H_2 and $CO_2/H_2/H_2O$ plasma; (d) In-situ OES results in CO_2/H_2 plasma, for plasma-only, plasma + CeO_2 support and plasma + Cu_2O/CeO_2 catalyst. (Pd in (b) is discharge power, input power = 23 W) .

Finally, we applied in-situ optical emission spectroscopy (OES) to detect important plasma species. Figure 2d illustrates several spectral lines and two spectral bands, including the H_a line (656.3 nm, $3d^2D \rightarrow 2p^2P^0$), the H_2 line (463 nm, $G^1å_g^+ \rightarrow B^1å_u^+$), two O atomic spectral lines (777.5 nm, $3s^5S^0 \rightarrow 3p^5P$ and 844.7 nm, $3s^3S^0 \rightarrow 3p^3P$), the CO band (450-580 nm, $B^1å \rightarrow A^1P$) and the H_2 band (580-650 nm, $d^3P_u \rightarrow a^3å_g^+$).[42,43] Clearly, plasma-only shows the highest signal intensity. Compared with plasma-only, the signal intensity is reduced by packing the CeO_2 support in the plasma, which is attributed to the shielding effect, and the signal intensity is further reduced by the Cu_2O/CeO_2 packing, indicating that some active species are adsorbed by the Cu_2O/CeO_2 catalyst. In addition, Figure S15a shows a decreasing signal intensity with increasing H_2O/CO_2 molar ratio. This is probably caused by ionization of H_2O, which consumes more energy, with correspondingly less energy to activate CO_2 and H_2, thereby leading to a drop in CO_2 conversion (Figures 1 b and d). Furthermore, the electronegativity of H_2O results in more electron attachment, indicating a lower density of free electrons in the plasma, and hence a lower production of reactive plasma species (Figure S15a), which may be another reason for the drop in CO_2 conversion.

To further verify the existence of OH radicals in the gas phase, OES measurements were conducted under plasma only conditions (Figure S15b). A distinct OH emission peak at 309.5 nm was observed, particularly at an H_2O/CO_2 molar ratio of 2, confirming the presence of OH radicals in the gas phase. The detection of OH radicals further supports their key role in driving surface reactions, such as CO_2 reduction and H_2 activation, under plasma conditions. The lifetime and density of OH radicals in plasma largely depend on the discharge mode and gas composition. Previous studies show that the density of OH radicals typically ranges from 10^{16}-10^{13} cm^{-3}, with 0.05%-1% H_2O content in the gas phase [44, 45], and their lifetime varies between 0.15 μs and 200 μs.[46, 47] In our study, the high content of H_2O (33.33%) and the intensive filamentary discharge likely lead to abundant OH radicals, with a lifetime sufficient to drive surface reactions via E-R and/or L-H mechanisms.

3.3 Characterization of Cu_2O/CeO_2 Catalyst. Powder X-ray diffraction (PXRD) patterns (Figure 3a) of the Cu_2O/CeO_2 catalyst and CeO_2 support are highly consistent, both for the fresh and spent catalysts, indicating that loading copper on the CeO_2 support does not affect the crystal structure of CeO_2. However, two weak diffraction peaks belonging to CuO, i.e., (111) and (-111) lattice plane, appear in the PXRD patterns of the Cu_2O/CeO_2 catalyst, which may be attributed to low loading of copper on the support (5 wt.% loading). The H_2-TPR (temperature-programmed reduction) profiles in Figure 3b display three different reduction peaks of copper oxide species (α, β and γ) in both fresh and spent catalysts. The α and β peaks are attributed to the reduction in highly dispersed CuO and Cu-O_x-Ce solid solutions, respectively. CeO_2 has been found to promote the reduction in highly dispersed CuO, i.e., the smaller the CuO particles, more easily can they be reduced.[48] The γ peak represents bulk CuO, which needs to be reduced at a higher temperature, indicates that most copper exists as large copper oxide particles.

We also characterized the Cu_2O/CeO_2 catalyst using HAADF-STEM and EDX mapping (Figure S16), which indicates low dispersion of copper on CeO_2. The particle size distribution of CuO in the Cu_2O/CeO_2 catalyst is illustrated in Figure S17 with an average CuO particle size of ca. 500 nm. This is consistent with PXRD and

H_2-TPR results of Figures 3a-b, and the reasons of poor dispersion could be attributed to low surface area of CeO_2 and high calcination temperature during catalyst preparation. The XPS result of Cu 2p (Figure 3c) illustrates that Cu species on the fresh catalyst are present in the form of CuO. On the spent catalyst, however, the Cu species change from CuO (934 and 953.8 eV) to Cu_2O (932.9 and 952.8 eV),[49] which may be caused by the reduction capability of H_2 plasma during the reaction (Table S3). The observed decrease in the intensity of Cu^{2+} satellite peaks (942.9 and 962.8 eV) on the spent catalyst also provides evidence for the transformation of CuO to Cu_2O. The Cu LMM Auger spectra, shown in Figure 3d, further demonstrate the formation of Cu_2O phase during the reaction.[50] However, the PXRD pattern only shows the CuO phase in spent Cu_2O/CeO_2 catalyst, which means that only the surface CuO layer is reduced to Cu_2O by H_2 plasma. Subsequently, Ar^+ is used to etch the spent Cu_2O/CeO_2 catalyst with a depth of ca. 10 nm. However, the XPS result of Cu 2p only shows Cu^+ species (Figure S18). Therefore, Cu_2O species could be the active sites of the Cu_2O/CeO_2 catalyst for CO_2 hydrogenation to C_2H_5OH.

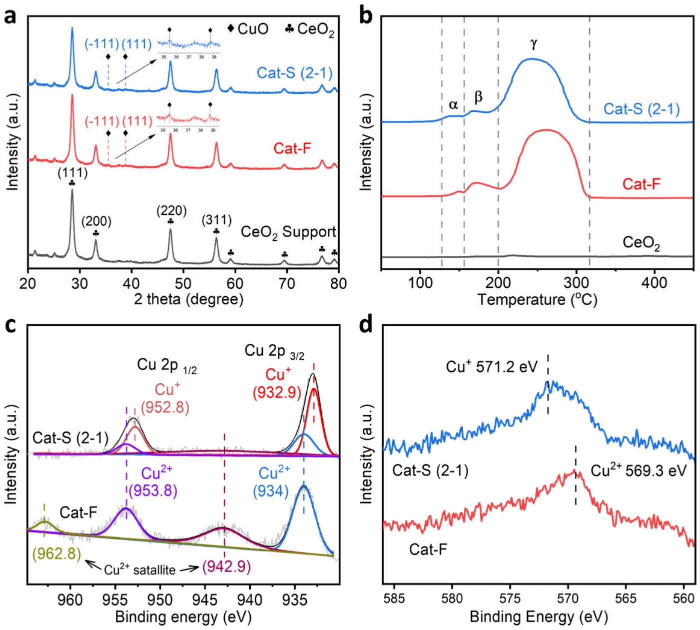

Figure 3. Characterization results of the Cu_2O/CeO_2 catalysts with 5 wt.% loading; (a) PXRD patterns; (b) H_2-TPR profiles; (c) Cu 2p XPS results; (d) Cu LMM Auger spectra. (Cat-F and Cat-S denote fresh and spent catalyst, respectively, and 2-1 denotes the molar ratio of H_2O/CO_2).

To further support above-mentioned conclusion, the fresh catalyst is first reduced by hydrogen to Cu^0 species, followed by its further use in CO_2 hydrogenation reaction. The Cu^0 species are oxidized to Cu^+ species (Figure S19), which can be attributed to the oxidizing properties of H_2O and CO_2. Although H_2 is a reducing gas, the gas temperature in the plasma is not sufficient to reduce Cu^+ to Cu^0. Previous reports came to the same conclusion that Cu^0 was not stable in H_2/CO_2 plasma at low temperature.[51] The above catalyst characterization results indicate that the surface Cu_2O layer of the Cu_2O/CeO_2 catalyst is the active phase for CO_2 hydrogenation to

C_2H_5OH. The N_2 physisorption data are shown in Figure S20 and Table S4, indicating that the BET surface area and pore volume of the Cu_2O/CeO_2 catalyst are very low. The spent Cu_2O/CeO_2 catalysts after plasma reaction with different H_2O content are further characterized by PXRD, H_2-TPR and XPS (Figure S21), and relevant results indicate that the content of H_2O during plasma-catalytic CO_2 hydrogenation does not have an obvious effect on the crystal phase and valence state of the spent Cu_2O/CeO_2 catalysts.

3.4 Isotope-tracing experiments. We used D_2O and $H_2{}^{18}O$ for isotope-tracing experiments to further determine the role of water in CO_2 hydrogenation. The mass spectra of the products from CO_2 hydrogenation in the presence of H_2O are shown in Figures S22 (a and b), which are highly consistent with the standard mass spectra of CH_3OH and C_2H_5OH.[52] Subsequently, trace amounts of CH_3OH and C_2H_5OH are added to a mixture of H_2O and D_2O (99% H_2O, 1% D_2O) as a control experiment to verify the H-D exchange reaction. As shown in Figures S22 (c and d), obvious H-D exchange reactions take place between the alcohols molecules and D_2O, resulting in the formation of CH_3OD and C_2H_5OD molecules, implying that the H-D exchange reaction mainly occurs between the OH group in the alcohols molecules and the D_2O molecule.

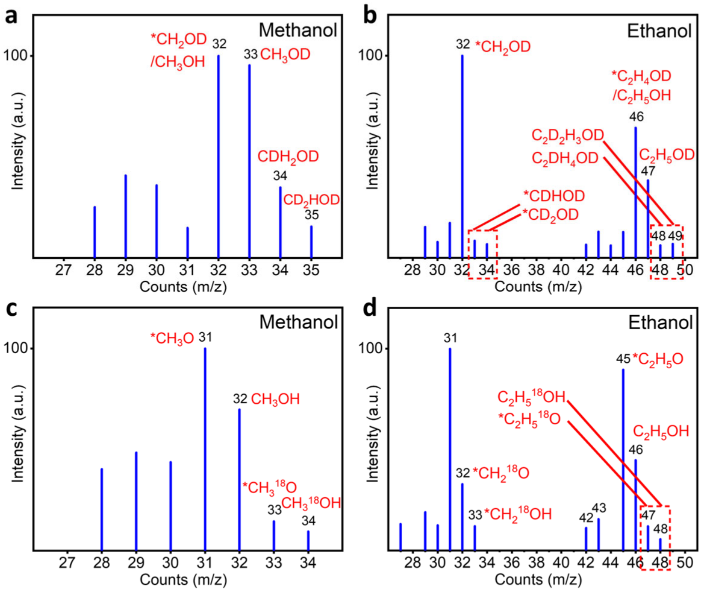

Figure 4. Isotope-tracing experimental results. (a, b) MS results of the products from CO_2 hydrogenation over Cu_2O/CeO_2 catalyst in the presence of D_2O; (c, d) MS results of the products from CO_2 hydrogenation over Cu_2O/CeO_2 catalyst in the presence of $H_2{}^{18}O$. Note that the m/z peaks for CH_3OH and C_2H_5OH typically correspond to different (fragmentation) species, hence the different assignments.

The mass spectra of the products from CO_2 hydrogenation in the presence of D_2O are shown in Figures 4 (a and b), revealing CDH_2OD, CD_2HO, C_2DH_4OD and $C_2D_2H_3OD$ among the products besides the expected products with only one D-atom, originating from the H-D exchange reaction in the OH-group of the alcohols. This means that D replaced two or more H atoms in the alcohols molecules, indicating that D atoms from D_2O dissociation are involved in the hydrogenation of CO_2, aside from the H-D exchange reaction. In other words, H from dissociation of H_2O should also be involved in the hydrogenation of CO_2 to CH_3OH and C_2H_5OH. In addition, the H_2/D_2O experiment demonstrates that H-D exchange also occurs between H_2 and D_2O (Figure S23). The mass spectra of products from CO_2 hydrogenation in the presence of $H_2{}^{18}O$ are shown in Figures 4 (c and d), indicating that $CH_3{}^{18}OH$ and $C_2H_5{}^{18}OH$ are detected in the products. This means that a proportion of the OH group in CH_3OH and C_2H_5OH is derived from OH species in H_2O molecule. Electron paramagnetic resonance (EPR) results (Figure S24) further confirm the dissociation of H_2O into OH radicals in both CO_2/H_2O and $H_2/CO_2/H_2O$ plasma systems. However, the OH signal is notably weaker in the presence of H_2 ($H_2/CO_2/H_2O$ plasma), suggesting that OH radicals are readily consumed under reducing conditions. However, the high content of H_2O likely facilitates a continuous dynamic process, where newly generated OH radicals from H_2O dissociation may compensate the consumed OH radicals, maintaining the observed signals. In short, the isotope-tracing results and EPR analysis demonstrate that water dissociates into H and OH species, actively participating in the CO_2 hydrogenation reaction under plasma conditions.

3.5 DFT calculations. A 6-layer Cu_2O (111) slab is built to simulate the C-C coupling and stepwise hydrogenation, as shown in Figure S25. Four typical sites, i.e., the surface-unsaturated Cu site (Cu_{cus}), saturated Cu site (Cu_{csa}), unsaturated O site (O_{cus}) and saturated O site (O_{csa}) are tested and the Cu_{cus} site is the most stable adsorption site for main reactants and intermediates. In this regard, the Cu_{cus} site is chosen as the active site for further reactions. The adsorption results and configurations are summarized in Table S5 and Figure S26.

Two typical C-C coupling mechanisms, i.e., CO* insertion into CH_3* and the combination between CH_xO*, are investigated.[10,15,53-55] The CO* insertion is found unfavorable in this system due to the limited production of CH_3*. A high barrier (2.05 eV) occurred in the decomposition of CH_3OH* to CH_3* and OH* (Figure S27). Besides, the energy barrier for CH_3* hydrogenation to CH_4* (1.40 eV) is lower than that for the formation of CH_3CO* (1.46 eV) by coupling with CO* (Figure S28). And the CH_3* generation from CO_2 hydrogenation and CH_4* dissociation is limited due to the low CH_4 selectivity (0.5% in this work) and the unfavorable route of CO_2 to CH_3* under plasma conditions.[56] Meanwhile, the barrier of CO*-CH_3* coupling is higher than most barriers in CH_xO*-CH_xO* coupling (Table S6). Accordingly, the C_2H_5OH formation via CO insertion mechanism on Cu_2O (111) is quite difficult.

Abundant H and CO signals in the OES spectrum indicate the possible generation of CH_xO species and their C-C coupling.[56] Six possible C-C coupling reactions between CH_xO are tested at their most favorable co-adsorption site, as shown in Figures 5 (a and b), Figure S29, Table S6 and Table S7. In contrast to the HCO-HCO coupling mechanism observed with the Cu-Cs catalyst,[55] the CO*-H_2CO* coupling in this study exhibits the lowest barrier of 0.91 eV over the Cu_{cus} site. Interestingly, only the H_2CO*-H_2CO* coupling shows an obvious C-C bonding (Figure S30), while other couplings show co-adsorption of two CH_xO* molecules, which could be attributed to the coordination status of C-C atoms.

Figure 1a shows the switch effect of the highest selectivity of alcohols from methanol to ethanol when H_2O/CO_2 ratio reaches 1. At this time, the amount of H_2O added is much higher than its yield from the hydrogenation. In plasma region, the H* dissociated from H_2O dissociation plays a similar role as H_2 for hydrogenation. Hence, OH* is assumed to be the main factor in promoting the production of C_2H_5OH. Two possible effects of hydroxyl groups, i.e. OH* pre-adsorption and the proton transfer, Inspired by Yang's work claiming that the catalyst surface is critical in CO_2 hydrogenation to C_2H_5OH,[57] are investigated. The pre-adsorbed OH* affects the C-C couplings. OH* favors the neighbor Cu_{cus} site when it co-adsorbs with C-C coupling species (Table S8 and Figure S31). OH* lowers the barrier in CO-H_2CO coupling from 0.91 to 0.85 eV while it increases the barrier in HCO-HCO coupling from 1.32 to 1.56 eV (Figure 5a). The pre-adsorption of OH* at a neighboring Cu_{cus} site slightly changes the charge distribution near H_2CO*, and promotes its migration to bind with CO* adsorbed Cu_{cus} (Table S9, Figures 5c-d, S32 and S33). In this regard, the pre-adsorption of OH* could to a certain extent promote the C-C coupling via CO-H_2CO, showing a much lower barrier than the other five C-C coupling pathways (Table S6).

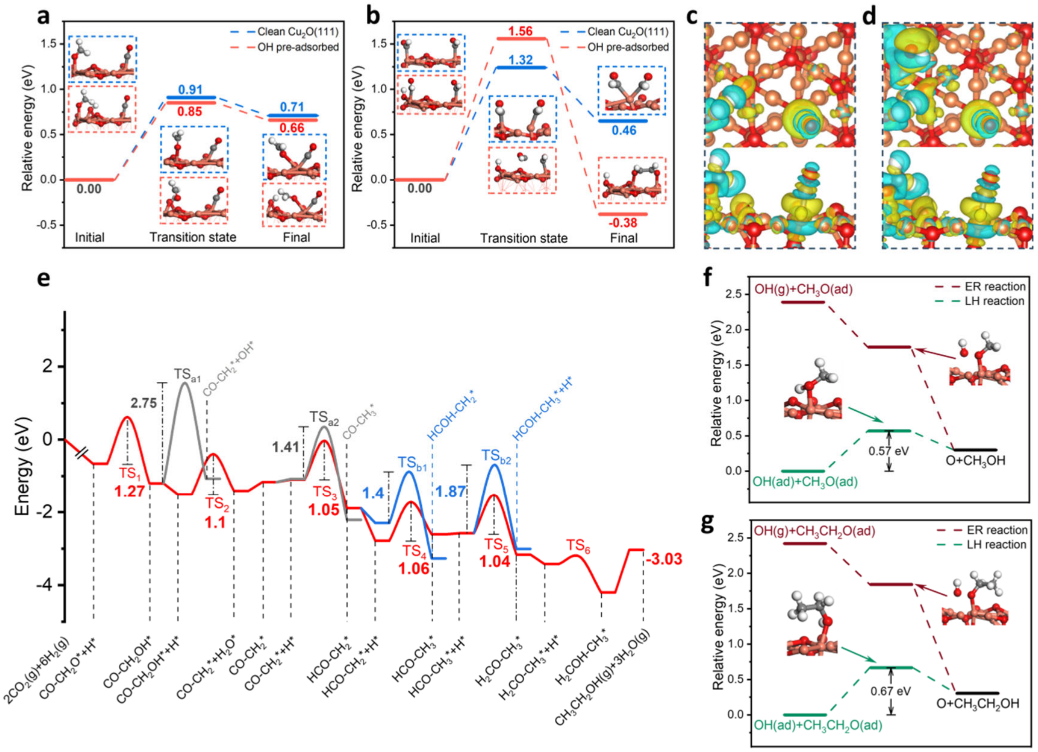

Figure 5. (a-e) DFT calculation results of C-C coupling. (a, b) Energy diagrams of C-C coupling at the Cucus sites on the surface of Cu_2O (111): (a) CO*-H_2CO*; (b) HCO*-HCO* coupling. (c-d) Partial charge distributions of (OH-)CO-H_2CO before coupling. (c) CO-H_2CO; (d) OH-CO-H_2CO. (e) Reaction pathway of C_2H_5OH formation from CO*-H_2CO* coupling (Adsorbed species are labeled as

). (f-g) Proton transfer of adsorbed OH or gas phase OH(g) to form (f) CH_3OH* and (g) C_2H_5OH*.

Considering CO*-H_2CO* as the main coupling way, the stepwise hydrogenation is shown in Figure 5e, with detailed information in Table S10. CO*-H_2CO* prefers to detach the O atom from -CH_2O via two hydrogenation steps to form H_2O, rather than via the direct decomposition of -CH_2OH* to CH_2* and OH* (E_a=2.75 eV). Subsequently, CO*-CH_2* prefers hydrogenation to HCO*-CH_2*(E_a=1.05 eV) rather CO*-CH_3* (E_a=1.41 eV). Further, H* is more likely to react with -CH_2* (E_a: 1.06 eV), rather than with -HCO* (E_a: 1.40 eV) in the HCO*-CH_2* complex. Subsequently, the CH_3*-HCO* complex receives two H* atoms to eventually form C_2H_5OH*. The C_2H_5OH* undergoes desorption to finalize the C_2H_5OH synthesis with a desorption energy of 1.17 eV. A compared path from HCO*-HCO* shows a higher rate-limiting step (1.60 eV) than the CO-H_2CO path (1.27 eV), as shown in Figure S34, which again proves the availability of the CO*-H_2CO* route.

According to isotope-tracing experiments, we proposed two possible reaction mechanisms for OH-induced alcohol synthesis. One is the proton transfer from OH to the alcohols. The other is the direct replacement of O in methoxyl and ethoxyl by OH. As shown in Figures 5 (f and g), the final steps of CH_3OH* and C_2H_5OH* formation are facilitated via the proton transfer. In the Langmuir-Hinshelwood (L-H) reactions, OH* co-adsorbs with CH_3O* or CH_3CH_2O* at the Cu_{cus} site, forming CH_3OH* and C_2H_5OH* with energy barriers of 0.57 and 0.67 eV, respectively. In the E-R reactions, the formation of CH_3OH* and C_2H_5OH* seems to have no obvious barrier due to the high reactivity of the OH(g) species. Besides, highly reactive gas-phase OH(g) species can move to the Cu_2O surface to react with CH_3O* or CH_3CH_2O*, forming CH_3OH* and O*, or C_2H_5OH* and O*, respectively. E_a values for these two reactions are high, i.e., 1.50 eV for CH_3OH and 1.62 eV for C_2H_5OH, respectively, due to the stable C-O bonds in both methoxyl or ethoxyl (Figures S35). The above results indicate the alcohol production promoted by OH radicals are more likely via the proton transfer.

Apart from the hydrogenation, the pre-adsorbed OH* is found to facilitate the C_2H_5OH desorption. As shown in Table S11, Figures S36 and S37. The co-adsorption of H_2O* and C_2H_5OH* is more stable when H_2O* is at the Cu_{cus} site, and then the C_2H_5OH* is unbonded. In this case, the adsorption energy of C_2H_5OH* is significantly reduced from -1.17 eV to -0.71 eV. By contrast, when C_2H_5OH* is adsorbed at the Cu_{cus} site, the H_2O molecule shows physisorption near the C_2H_5OH*, and the adsorption energy of C_2H_5OH is slightly reduced to -1.13 eV. Meanwhile, the competitive adsorption of OH* at neighboring sites can easily get involved in the next C-C coupling and in proton transfer processes after the desorption of C_2H_5OH.

Generally, H_2O acts as a “switch” in guiding the CO_2 hydrogenation from methanol to ethanol in Cu-based plasma-catalytic system. The multiple roles of H_2O on C_2H_5OH synthesis, namely C-C coupling enhancement, proton transfer and desorption promotion, offers a competitive approach of green-chemical synthesis at room temperature and atmospheric pressure with distributed power supply.[58,59] Additionally, the presence of water vapor stabilizes methanol and ethanol, shortening their residence time in the plasma phase by reducing their interaction with highly reactive plasma species, thereby preventing excessive decomposition. We note that the oxide-support interaction for Cu_2O-CeO_2 might also be a factor affecting the CO_2 hydrogenation and alcohols selectivity.[60] However, in this work, the bulk CuO particle size is found to be very large and the dispersion is very poor, leaving limited Cu-CeO_2 interfacial sites for possible reactions. Meanwhile, the CeO_2 alone does not show a superior improvement in CO_2 conversion performance compared with other oxides (Figure S9). In this regard, unlike H_2O addition, the CeO_2 support might not be a determining factor in guiding the C-C coupling and hydrogenation.

In this study, the energy consumption for the synthesis of alcohols was determined to be approximately 16.4 kJ/mmol, being significantly higher than the heating value of ethanol as a fuel (~1.23 kJ/mmol). The low energy efficiency of our system is likely attributed to inherent energy losses during plasma activation, including ineffective collisions and recombination of reactive species, as well as the generation of by-products such as CO and CH_4. Future improvements could focus on optimizing catalysts for higher ethanol selectivity, refining reactor designs to minimize energy dissipation, and integrating energy recovery systems. Addressing these challenges is essential for advancing the viability of plasma-catalytic CO_2 hydrogenation.

4. CONCLUSIONS

We demonstrated the synergy between plasma and Cu_2O/CeO_2 catalyst in CO_2 hydrogenation to alcohols with assistance of H_2O. The non-thermal plasma enables the conversion of small molecules (CO_2, H_2, H_2O, etc.) over Cu_2O/CeO_2 catalyst under mild conditions, achieving a high C_2H_5OH selectivity of 56% at atmospheric pressure and ~75 °C. The addition of water improves energy efficiency by over 32 times compared to using plasma alone and the dissociated H and OH from H_2O are found engaged in the CO_2 hydrogenation. DFT calculations suggest that the C-C coupling via CO-H_2CO combination is most likely to happen at unsaturated Cu_{cus} site with OH pre-adsorption over the Cu_2O (111) surface. Meanwhile, the OH species could promote the stepwise hydrogenation due to the proton transfer via both L-H and E-R mechanism. The competitive adsorption of H_2O and OH improve the alcohols desorption by “seizing” the Cu_{cus} sites. In summary, the triple role of H_2O on the alcohols production, specifically the promotion on C-C coupling, hydrogenation and alcohols desorption, makes it a switch in controlling the alcohols generation from CH_3OH to C_2H_5OH. And new insights in this work enable a better understanding on CO_2 conversion to higher alcohols in plasma-catalysis.

ASSOCIATED CONTENT

*Supporting Information

The Supporting Information is available free of charge at https://pubs.acs.org/doi/XX

Quantitative analysis of reaction results; schematic diagram of the experimental setup; summary of CO_2 hydrogenation to C_2H_5OH with various catalysts and catalytic methods; plasma diagnoses data (temperature distribution by IR camera, discharge parameters by oscilloscope, active species by OES); reaction performance data (GC profiles, control experiments); carbon balance calculations; stability tests; energy consumption data; catalyst characterization data (HAADF-STEM, XPS, N_2 adsorption, TPR, GC-MS, isotope tracer, EPR); electronic energy distribution function; DFT calculation results.

AUTHOR INFORMATION

Corresponding Author

Yanhui Yi - *State Key Laboratory of Fine Chemicals, School of Chemical Engineering, Dalian University of Technology, Dalian 116024, China*
Email: yiyanhui@dlut.edu.cn
An-Hui Lu - *State Key Laboratory of Fine Chemicals, School of Chemical Engineering, Dalian University of Technology, Dalian 116024, China*
Email: anhuilu@dlut.edu.cn
Yi Liu - *State Key Laboratory of Fine Chemicals, School of Chemical Engineering, Dalian University of Technology, Dalian 116024, China*
Email: diligenliu@dlut.edu.cn
Min Liu - *State Key Laboratory of Powder Metallurgy, School of Physics, Central South University, Changsha 410083, China*
Email: minliu@csu.edu.cn

Authors

Shengyan Meng - *State Key Laboratory of Fine Chemicals, School of Chemical Engineering, Dalian University of Technology, Dalian 116024, China*
Zhaolun Cui - *Key Lab of Materials Modification by Laser, Ion, and Electron Beams, Dalian University of Technology, Dalian 116024, China; Key Lab of Materials Modification by Laser, Ion, and Electron Beams, Dalian University of Technology, Dalian 116024, China*
Qian Chen - *State Key Laboratory of Fine Chemicals, School of Chemical Engineering, Dalian University of Technology, Dalian 116024, China*
Hang Zhang - *State Key Laboratory of Powder Metallurgy, School of Physics and Electronics, Central South University, Changsha 410083, China*
Shangkun Li - *Research group PLASMANT, Department of Chemistry, University of Antwerp, Universiteitsplein 1, BE-2610 Wilrijk-Antwerp, Belgium*
Erik C Neyts - *Research group PLASMANT, Department of Chemistry, University of Antwerp, Universiteitsplein 1, BE-2610 Wilrijk-Antwerp, Belgium*
Evgenii Vlasov - *Electron Microscopy for Materials Science (EMAT), University of Antwerp, Groenenborgerlaan 171, BE-2020 Wilrijk-Antwerp, Belgium*
Kellie Jenkinson - *Electron Microscopy for Materials Science (EMAT), University of Antwerp, Groenenborgerlaan 171, BE-2020 Wilrijk-Antwerp, Belgium*
Sara Bals - *Electron Microscopy for Materials Science (EMAT), University of Antwerp, Groenenborgerlaan 171, BE-2020 Wilrijk-Antwerp, Belgium*

Dezheng Yang - *Key Lab of Materials Modification by Laser, Ion, and Electron Beams, Dalian University of Technology, Dalian 116024, China*
Annemie Bogaerts - *Research group PLASMANT, Department of Chemistry, University of Antwerp, Universiteitsplein 1, BE-2610 Wilrijk-Antwerp, Belgium*

Notes
The authors declare no competing financial interest.

ACKNOWLEDGEMENTS

This work was supported by the National Natural Science Foundation of China [22272015, 22472018, 21503032], the European Research Council (ERC) under the European Union's Horizon 2020 research and innovation programme (ERC Synergy Grant 810182 SCOPE and 823717 ESTEEM3), and the Methusalem project at Universiteit Antwerpen. Computational resources were provided by the HPC core facility CalcUA of the Universiteit Antwerpen, and VSC (Flemish Supercomputer Center).

REFERENCES

(1) Von der Assen, N.; Voll, P.; Peters, M.; Bardow, A., Life cycle assessment of CO_2 capture and utilization: a tutorial review. *Chem. Rev.* **2014**, *43*, 7982-7994.
(2) Porosoff, M. D.; Yang, X.; Boscoboinik, J. A.; Chen, J. G., Molybdenum Carbide as Alternative Catalysts to Precious Metals for Highly Selective Reduction of CO_2 to CO. *Angew. Chem. Int. Ed.* **2014**, *53*, 6705-6709.
(3) Xu, D.; Wang, Y.; Ding, M.; Hong, X.; Liu, G.; Tsang, S. C. E., Advances in higher alcohol synthesis from CO_2 hydrogenation. *Chem* **2021**, *7*, 849-881.
(4) Li, Z.; Wang, J.; Qu, Y.; Liu, H.; Tang, C.; Miao, S.; Feng, Z.; An, H.; Li, C., Highly Selective Conversion of Carbon Dioxide to Lower Olefins. *ACS Catal.* **2017**, *7*, 8544-8548.
(5) Ni, Y. M.; Chen, Z. Y.; Fu, Y.; Liu, Y.; Zhu, W. L.; Liu, Z. M., Selective conversion of CO_2 and H_2 into aromatics. *Nat. Commu.* **2018**, *9, 3457*.
(6) Zhong, J.; Yang, X.; Wu, Z.; Liang, B.; Huang, Y.; Zhang, T., State of the art and perspectives in heterogeneous catalysis of CO_2 hydrogenation to methanol. *Chem. Soc. Rev.* **2020**, *49*, 1385-1413.
(7) Sun, J.; Wang, Y., Recent Advances in Catalytic Conversion of Ethanol to Chemicals. *ACS Catal.* **2014**, *4*, 1078-1090.
(8) Inoue, T.; Iizuka, T.; Tanabe, K. Hydrogenation of Carbon Dioxide and Carbon Monoxide over Supported Rhodium Catalysts under 10 Bar Pressure. *Appl. Catal. A* **1989**, *46*, 1-9.
(9) Wang, D.; Bi, Q.; Yin, G.; Wang, P.; Huang, F.; Xie, X.; Jiang, M., Photochemical Preparation of Anatase Titania Supported Gold Catalyst for Ethanol Synthesis from CO_2 Hydrogenation. *Catal. Lett.* **2018**, *148*, 11-22.

(10) He, Z.; Qian, Q.; Ma, J.; Meng, Q.; Zhou, H.; Song, J.; Liu, Z.; Han, B., Water-Enhanced Synthesis of Higher Alcohols from CO_2 Hydrogenation over a Pt/Co_3O_4 Catalyst under Milder Conditions. *Angew. Chem. Int. Ed.* **2016**, *55*, 737-741.

(11) Bai, S.; Shao, Q.; Wang, P.; Dai, Q.; Wang, X.; Huang, X., Highly Active and Selective Hydrogenation of CO_2 to Ethanol by Ordered Pd-Cu Nanoparticles. *J. Am. Chem. Soc.* **2017**, *139*, 6827-6830.

(12) Wang, L.; Wang, L.; Zhang, J.; Liu, X.; Wang, H.; Zhang, W.; Yang, Q.; Ma, J.; Dong, X.; Yoo, S. J.; Kim, J.-G.; Meng, X.; Xiao, F.-S., Selective Hydrogenation of CO_2 to Ethanol over Cobalt Catalysts. *Angew. Chem. Int. Ed.* **2018**, *57*, 6104-6108.

(13) Yang, C.; Liu, S.; Wang, Y.; Song, J.; Wang, G.; Wang, S.; Zhao, Z.-J.; Mu, R.; Gong, J., The Interplay between Structure and Product Selectivity of CO_2 Hydrogenation. *Angew. Chem. Int. Ed.* **2019**, *58*, 11242-11247.

(14) Ding, L.; Shi, T.; Gu, J.; Cui, Y.; Zhang, Z.; Yang, C.; Chen, T.; Lin, M.; Wang, P.; Xue, N.; Peng, L.; Guo, X.; Zhu, Y.; Chen, Z.; Ding, W., CO_2 Hydrogenation to Ethanol over Cu@Na-Beta. *Chem* **2020**, *6*, 2673-2689.

(15) Zhang, S.; Liu, X.; Shao, Z.; Wang, H.; Sun, Y., Direct CO_2 hydrogenation to ethanol over supported Co_2C catalysts: Studies on support effects and mechanism. *J. Catal.* **2020**, *382*, 86-96.

(16) Zhang, S.; Wu, Z.; Liu, X.; Shao, Z.; Xia, L.; Zhong, L.; Wang, H.; Sun, Y., Tuning the interaction between Na and Co_2C to promote selective CO_2 hydrogenation to ethanol. *Appl. Catal., B* **2021**, *293, 120207*.

(17) Jiang, X.; Nie, X.; Gong, Y.; Moran, C. M.; Wang, J.; Zhu, J.; Chang, H.; Guo, X.; Walton, K. S.; Song, C., A combined experimental and DFT study of H_2O effect on In_2O_3/ZrO_2 catalyst for CO_2 hydrogenation to methanol. *J. Catal.* **2020**, 383, 283-296.

(18) Wang, Y.; Gao, W.; Li, K.; Zheng, Y.; Xie, Z.; Na, W.; Chen, J. G.; Wang, H., Strong Evidence of the Role of H_2O in Affecting Methanol Selectivity from CO_2 Hydrogenation over $Cu\text{-}ZnO\text{-}ZrO_2$. *Chem* **2020**, 6, 419-430.

(19) Graciani, J.; Grinter, C.; Ramírez, J.; Palomino, R.; Xu, F.; Waluyo, I.; Stacchiola, D.; Sanz, J.; Senanayake, S.; Rodriguez, J., Conversion of CO_2 to Methanol and Ethanol on $Pt/CeO_x/TiO_2$ (110): Enabling Role of Water in C-C Bond Formation. *ACS Catal.* **2022**, 12, 15097-15109.

(20) Cui, Z.; Meng, S.; Yi, Y.; Jafarzadeh, A.; Li, S.; Neyts, E. C.; Hao, Y.; Li, L.; Zhang, X.; Wang, X.; Bogaerts, A., Plasma-Catalytic Methanol Synthesis from CO_2 Hydrogenation over a Supported Cu Cluster Catalyst: Insights into the Reaction Mechanism. *ACS Catal.* **2022**, 12, 1326-1337.

(21) Silva, A. H. M. d.; Vieira, L. H.; Santanta, C. S.; Koper, M. T. M.; Assaf, E. M.; Assaf, J. M.; Gomes, J. F., Ethanol formation from CO_2 hydrogenation at atmospheric pressure using Cu catalysts: Water as a key component. *Appl. Catal., B* **2023**, 324, 122221.

(22) Snoeckx, R.; Bogaerts, A., Plasma technology-a novel solution for CO_2 conversion? *Chem. Soc. Rev.* **2017**, 46, 5805-5863.

(23) Kim, D. Y.; Ham, H.; Chen, X.; Liu, S.; Xu, H.; Lu, B.; Furukawa, S.; Kim, H. H.; Takakusagi, S.; Sasaki, K.; Nozaki, T. Cooperative catalysis of vibrationally

excited CO_2 and alloy catalyst breaks the thermodynamic equilibrium limitation. *J. Am. Chem. Soc.* **2022**, 144, 14140-14149.

(24) Gao, X. Y.; Liang, J. L.; Wu, L. Q.; Wu, L. X.; Kawi, S., Dielectric Barrier Discharge Plasma-Assisted Catalytic CO_2 Hydrogenation: Synergy of Catalyst and Plasma. *Catalysts* **2022**, 12, 66.

(25) Xu, S.; Chen, H.; Fan, X., Rational design of catalysts for non-thermal plasma (NTP) catalysis: A reflective review. *Catal. Today* **2023**, 419, 114144.

(26) Bogaerts, A.; Tu, X.; Whitehead, J C.; Centi, G.; Lefferts, L.; Guaitella, O.; Azzolina-Jury, F.; Kim, H H.; Murphy, A.; Schneider, W.; Nozaki, T.; Hicks, J.; Rousseau, A.; Thevenet, F.; Khacef, A.; Cerreon, M., The 2020 plasma catalysis roadmap. *J. Phys. D: Appl. Phys.* **2020**, *53*, 443001.

(27) Shirazi, M.; Neyts, E. C.; Bogaerts, A. DFT study of Ni-catalyzed plasma dry reforming of methane. *Appl. Catal., B* **2017**, *205*, 605-614.

(28) Hutter, J.; Iannuzzi, M.; Schiffmann, F.; VandeVondele, J., CP2K: atomistic simulations of condensed matter systems. Wiley Interdiscip. *Rev. Comput. Mol. Sci.* **2014**, *4*, 15-25.

(29) VandeVondele, J.; Krack, M.; Mohamed, F.; Parrinello, M.; Chassaing, T.; Hutter, J., QUICKSTEP: Fast and accurate density functional calculations using a mixed Gaussian and plane waves approach. *Comput. Phys. Commun.* **2005**, *167*, 103-128

(30) VandeVondele, J.; Hutter, J., Gaussian basis sets for accurate calculations on molecular systems in gas and condensed phases. J. Chem. Phys. **2007**, *127*, 114105.

(31) Goedecker, S.; Teter, M.; Hutter, J., Separable dual-space Gaussian pseudopotentials. *Phys. Rev. B.* **1996**, *54*, 1703-1710.

(32) Grimme, S.; Ehrlich, S.; Goerigk, L., Effect of the Damping Function in Dispersion Corrected Density Functional Theory. *J. Comput. Chem.* **2011**, *32*, 1456-1465.

(33) Grimme, S.; Antony, J.; Ehrlich, S.; Krieg, H., A consistent and accurate ab initio parametrization of density functional dispersion correction (DFT-D) for the 94 elements H-Pu. *J. Chem. Phys.* **2010**, *132*, 154104.

(34) Bal, K. M.; Huygh, S.; Bogaerts, A.; Neyts, E. C., Effect of plasma-induced surface charging on catalytic processes: application to CO_2 activation. *Plasma Sources Sci. Technol.* **2018**, *27*, 024001.

(35) Henkelman, G.; Uberuaga, B. P.; Jonsson, H., A climbing image nudged elastic band method for finding saddle points and minimum energy paths. *J. Chem. Phys.* **2000**, *113*, 9901-9904.

(36) Song, Y.-Y.; Wang, G.-C., A DFT Study and Microkinetic Simulation of Propylene Partial Oxidation on CuO (111) and CuO (100) Surfaces. *J. Phys. Chem. C.* **2016**, *120*, 27430-27442.

(37) Lustemberg, P. G.; Palomino, R. M.; Gutierrez, R. A.; Grinter, D. C.; Vorokhta, M.; Liu, Z.; Ramirez, P. J.; Matolin, V.; Veronica Ganduglia-Pirovano, M.; Senanayake, S. D.; Rodriguez, J. A., Direct Conversion of Methane to Methanol on Ni-Ceria Surfaces: Metal-Support Interactions and Water-Enabled Catalytic Conversion by Site Blocking. *J. Am. Chem. Soc.* **2018**, *140*, 7681-7687.

(38) Butterworth, T.; Allen, R. W. K., Plasma-catalyst interaction studied in a single

pellet DBD reactor: dielectric constant effect on plasma dynamics. *Plasma Sources Sci. Technol.* **2017**, *26*, 065008.

(39) Hagelaar, G. J. M.; Pitchford, L. C., Solving the Boltzmann equation to obtain electron transport coefficients and rate coefficients for fluid models. *Plasma Sources Sci. Technol.* **2005**, *14*, 722-733.

(40) Mei, D. H.; Zhu, X. B.; He, Y. L.; Yan, J. D.; Tu, X., Plasma-assisted conversion of CO_2 in a dielectric barrier discharge reactor: understanding the effect of packing materials. *Plasma Sources Sci. Technol.* **2015**, *24*, 015011.

(41) Van Laer, K.; Bogaerts, A., Fluid modelling of a packed bed dielectric barrier discharge plasma reactor. *Plasma Sources Sci. Technol.* **2016**, *25*, 015002.

(42) Meng, S.; Wu, L.; Liu, M.; Cui, Z.; Chen, Q.; Li, S.; Yan, J.; Wang, L.; Wang, X.; Qian, J.; Guo, H.; Niu, J.; Bogaerts, A.; Yi, Y., Plasma-driven CO_2 hydrogenation to CH_3OH over Fe_2O_3/γ-Al_2O_3 catalyst. *AIChE J.* **2023**, e18154.

(43) Chen, Q.; Meng, S.; Liu, R.; Zhai, X.; Wang, X.; Wang, L.; Guo, H.; Yi, Y., Plasma-catalytic CO_2 hydrogenation to methanol over CuO-MgO/Beta catalyst with high selectivity. *Appl. Catal., B* **2024**, 342, 123422.

(44) Benedikt, J.; Schroeder, D.; Schneider, S.; Willems, G.; Pajdarova, A.; Vlcek, J.; Schulz-von der Gathen, V., Absolute OH and O radical densities in effluent of a He/H2O micro-scaled atmospheric pressure plasma jet. *Plasma Sources Sci. T.* **2016**, 25, 045013.

(45) Li, D.; Nikiforov, A.; Britun, N.; Snyders, R.; Kong, M. G.; Leys, C., OH radical production in an atmospheric pressure surface micro-discharge array. *J. Phys. D: Appl. Phys.* **2016**, 49, 455202.

(46) Piskarev, I. M., The Formation of Ozone-Hydroxyl Mixture in Corona Discharge and Lifetime of Hydroxyl Radicals. *IEEE Trans. Plasma Sci.* **2021**, 49, 1363-1372.

(47) Pei, X.; Lu, Y.; Wu, S.; Xiong, Q.; Lu, X., A study on the temporally and spatially resolved OH radical distribution of a room-temperature atmospheric-pressure plasma jet by laser-induced fluorescence imaging. *Plasma Sources Sci. T.* **2013**, 22, 025023.

(48) He, C.; Yu, Y.; Yue, L.; Qiao, N.; Li, J.; Shen, Q.; Yu, W.; Chen, J.; Hao, Z., Low-temperature removal of toluene and propanal over highly active mesoporous $CuCeO_x$ catalysts synthesized via a simple self-precipitation protocol. *Appl. Catal., B* **2014**, *147*, 156-166.

(49) Zhang, X. L.; Li, G. J.; Tian, R. L.; Feng, W. J.; Wen, L., Monolithic porous CuO/CeO_2 nanorod composites prepared by dealloying for CO catalytic oxidation. *J. Alloys Compd.* **2020**, 826, 154149.

(50) Platzman, I.; Brener, R.; Haick, H.; Tannenbaum, R., Oxidation of polycrystalline copper thin films at ambient conditions. *J. Phys. Chem. C* **2008**, 112, *4*, 1101-1108.

(51) Zhao, B.; Liu, Y.; Zhu, Z.; Guo, H.; Ma, X., Highly selective conversion of CO_2 into ethanol on $Cu/ZnO/Al_2O_3$ catalyst with the assistance of plasma. *J. CO_2 Util.* **2018**, *24*, 34-30.

(52) Nixon, K. L.; Pires, W. A. D.; Neves, R. F. C.; Duque, H. V.; Jones, D. B.; Brunger, M. J.; Lopes, M. C. A., Electron impact ionisation and fragmentation of

methanol and ethanol. *Int. J. Mass Spectrom* **2016**, 404, 48-59.

(53) Wang, G.; Luo, R.; Yang, C.; Song, J.; Xiong, C.; Tian, H.; Zhao, Z.-J.; Mu, R.; Gong, J., Active sites in CO_2 hydrogenation over confined VO_x-Rh catalysts. *Sci. China Chem.* **2019**, *62*, 1710-1719.

(54) Lou, Y.; Jiang, F.; Zhu, W.; Wang, L.; Yao, T.; Wang, S.; Yang, B.; Yang, B.; Zhu, Y.; Liu, X., CeO_2 supported Pd dimers boosting CO_2 hydrogenation to ethanol. *Appl. Catal., B* **2021**, *291*, 120122.

(55) Wang, X.; Ramirez, P. J.; Liao, W.; Rodriguez, J. A.; Liu, P., Cesium-Induced Active Sites for C-C Coupling and Ethanol Synthesis from CO_2 Hydrogenation on Cu/ZnO(0001) Surfaces. *J. Am. Chem. Soc.* **2021**, *143*, 13103-13112.

(56) De Bie, C.; van Dijk, J.; Bogaerts, A., CO_2 Hydrogenation in a Dielectric Barrier Discharge Plasma Revealed. *J. Phys. Chem. C* **2016**, *120*, 25210-25224.

(57) Yang, C.; Mu, R.; Wang, G.; Song, J.; Tian, H.; Zhao, Z.-J.; Gong, J., Hydroxyl-mediated ethanol selectivity of CO_2 hydrogenation. *Chem. Sci.* **2019**, *10*, 3161-3167.

(58) Zhang, S.; Gao, Y.; Sun, H.; Fan, Z.; Shao, T., Dry reforming of methane by microsecond pulsed dielectric barrier discharge plasma: optimizing the reactor structures. *High Volt.* **2022**, *7*, 718-729.

(59) Zhang, S.; Gao, Y.; Sun, H.; Fan, Z.; Shao, T., Charge transfer in plasma assisted dry reforming of methane using a nanosecond pulsed packed-bed reactor discharge. *Plasma Sci. Tech.* **2021**, *23*, 064007.

(60) Liu, Z.; Huang, E.; Orozco, I.; Liao, W.; Palomino, R. M.; Rui, N.; Duchon, T.; Nemsak, S.; Grinter, D. C.; Mahapatra, M.; Liu, P.; Rodriguez, J. A.; Senanayake, S.D., Water-promoted interfacial pathways in methane oxidation to methanol on a CeO_2-Cu_2O catalyst. *Science* **2020**, 368, 513-517.

TOC graphic

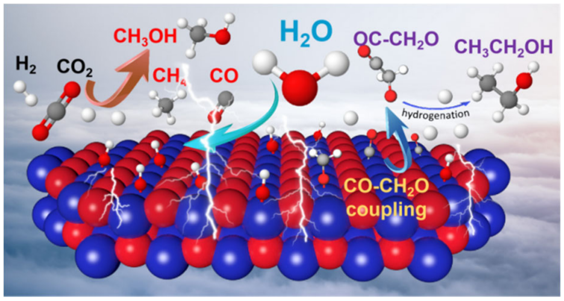
H_2
CO_2
CH_3OH
CH_4
CO
H_2O
$OC\text{-}CH_2O$
CH_3CH_2OH
hydrogenation
$CO\text{-}CH_2O$ coupling

Supporting Information

Water-Promoted C-C Coupling Reaction in Plasma-catalytic CO_2 Hydrogenation for Ethanol Production

Shengyan Meng[1†], Zhaolun Cui[2,6†], Qian Chen[1†], Hang Zhang[3], Shangkun Li[4], Erik Cornelis Neyts[4], Evgenii Vlasov[5], Kellie Jenkinson[5], Sara Bals[5], Dezheng Yang[2], Min Liu[3,*], Yi Liu[1,*], Annemie Bogaerts[4], An-Hui Lu[1,*] and Yanhui Yi[1,*]

[1]State Key Laboratory of Fine Chemicals, School of Chemical Engineering, Dalian University of Technology, Dalian 116024, China;
[2]School of Electric Power Engineering, South China University of Technology, Guangzhou 510630, China;
[3]State Key Laboratory of Powder Metallurgy, School of Physics, Central South University, Changsha 410083, China;
[4]Research group PLASMANT, Department of Chemistry, University of Antwerp, Universiteitsplein 1, BE-2610 Wilrijk-Antwerp, Belgium;
[5]Electron Microscopy for Materials Science (EMAT), University of Antwerp, Universiteitsplein 1, BE-2610 Wilrijk-Antwerp, Belgium;
[6]School of Electric Power Engineering, South China University of Technology, Guangzhou 510630, China;

†: S.M., Z.C. and Q.C. contributed equally to this paper

Corresponding author. E-mail addresses: yiyanhui@dlut.edu.cn (Y.H. Yi), anhuilu@dlut.edu.cn (A.H. Lu), diligenliu@dlut.edu.cn (Y. Liu), minliu@csu.edu.cn (M. Liu).

Quantitative analysis

In our work, the CO_2 conversion is defined as Eq. (1),

$$X(CO_2) = \frac{n(CO_2)_{in} - n(CO_2)_{out}}{n(CO_2)_{in}} \times 100\% \quad (1)$$

where $n(CO_2)_{in}$ and $n(CO_2)_{out}$ represent the molar content of CO_2 entering and exiting per minute, respectively. The molar content is determined by the product of concentration and total gas flow rate.

The selectivity of CO and CH_4 is defined as Eq. (2) and Eq. (3), respectively.

$$S(CO) = \frac{n(CO)_{out}}{n(CO_2)_{in} - n(CO_2)_{out}} \times 100\% \quad (2)$$

$$S(CH_4) = \frac{n(CH_4)_{out}}{n(CO_2)_{in} - n(CO_2)_{out}} \times 100\% \quad (3)$$

where $n(CO)_{out}$ and $n(CH_4)_{out}$ *(mol)* represent the molar content of CO and CH_4 in the exhaust gas per minute, respectively.

In the condensed liquid, only CH_3OH and C_2H_5OH were detected. Small amounts of isopropanol were detected at certain experiments, but their concentrations were negligible compared to the other products (isopropanol selectivity less than 0.2%). Also, there was no carbon deposition (coking) on the catalyst after the reaction. When water is not added in the reaction, the selectivity of liquid products is determined by Eq. (4). However, under the conditions where water is added, the selectivity of the liquid products can be calculated as Eq. (5) and Eq. (6), respectively. (The differences in the analysis formulas are explained in Figure S7)

$$S(Alcohols) = 100\% - S(CO) - S(CH_4) \quad (4)$$

$$S(CH_3OH) = \frac{c(CH_3OH) \times V(Liquid)}{n(CO_2)_{in} - n(CO_2)_{out}} \times 100\% \quad (5)$$

$$S(C_2H_5OH) = \frac{2c(C_2H_5OH) \times V(Liquid)}{n(CO_2)_{in} - n(CO_2)_{out}} \times 100\% \quad (6)$$

where *V(Liquid)* represents the volume of collected liquid products, and $c(CH_3OH)$ and $c(C_2H_5OH)$ represent the molar concentrations of CH_3OH and C_2H_5OH in the liquid products, respectively. The factor 2 before $c(C_2H_5OH)$ stands for the coefficient of conversion of two CO_2 molecules into one C_2H_5OH molecule.

$$Energy\ consumption(kJ/mmol) = \frac{discharge\ power\ \ (J/s)}{v(CH_3OH) + 2v(C_2H_5OH)\ (mol/s)} \times 10^{-6} \quad (7)$$

where $v(CH_3OH)$ *and* $v(C_2H_5OH)$ *(mol/s)* represent the production rate of CH_3OH and C_2H_5OH, respectively. The factor 10^{-6} is needed to convert J/mol into kJ/mmol.

The discharge power is calculated by the voltage-charge Lissajous graphic method. A measuring capacitor C_m *(F)* is connected in series with a grounding electrode. The value of the capacitance is known and much higher than the equivalent capacitance of the reactor. The current calculation formula of the loop is defined as Eq. (8),

$$I = C_m \frac{dU_m}{dt} \tag{8}$$

where C_m *(F)* is the measured capacitance, and U_m *(V)* is the voltage across the measured capacitance.

The discharge power of a single cycle can be obtained by definite integration of the input voltage and the current flowing through the electrode, as shown in Eq. (9),

$$P = \frac{1}{T}\int_0^T UIdt = \frac{C_m}{T}\int_0^T U\frac{dU_m}{dt}dt = fC_m \oint UdU_m \tag{9}$$

where T *(s)* is the discharge period, U *(V)* is the voltage applied between the electrodes and f *(Hz)* is the discharge frequency.

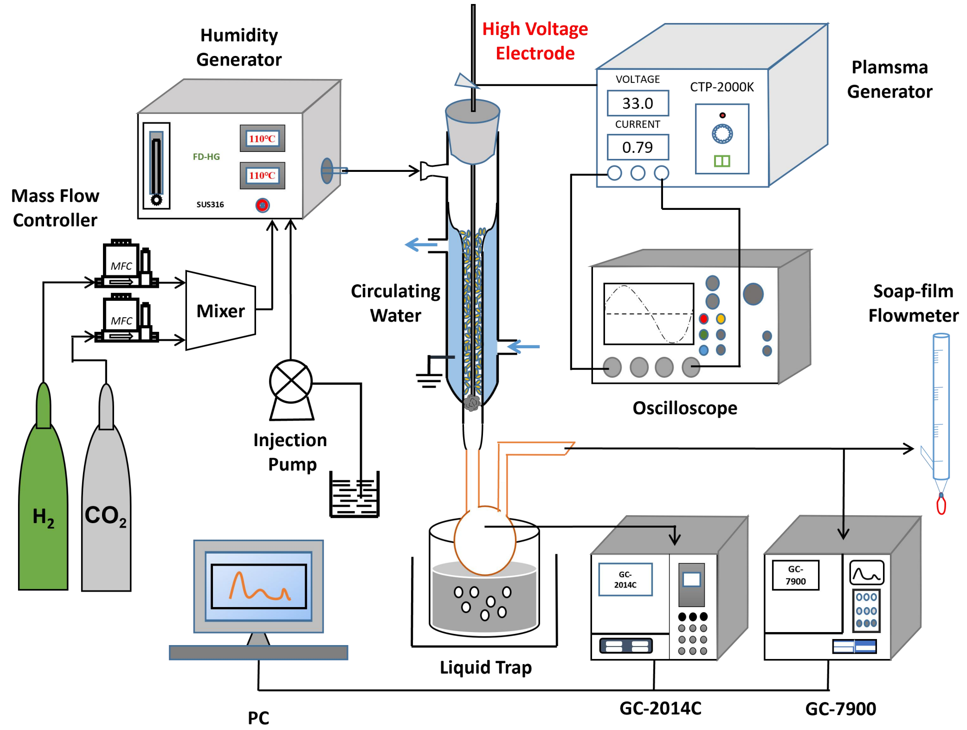

Scheme S1 Schematic diagram of the experimental setup.

Summary of CO_2 hydrogenation to C_2H_5OH under different catalysts and catalytic modes

Table S1 summarizes the CO_2 conversion, C_2H_5OH selectivity and energy consumption obtained by plasma catalysis in our study, for various CO_2/H_2O molar ratios, in comparison to the performance achieved by thermal catalysis and electrocatalysis in the literature for CO_2 hydrogenation to C_2H_5OH, using various catalysts (as indicated in the first column, along with the references). It is evident that the majority of reported catalysts, evaluated in fixed-bed reactors, struggle with poor C_2H_5OH selectivity. While tank reactors (denoted with * in Table S1) offer distinct advantages in terms of product selectivity within a closed recirculating environment, they face batch issues, hindering continuous operation. Electrocatalytic CO_2 reduction is attractive due to its modular system and high Faradaic efficiency. However, it comes with its own set of challenges, including the low solubility of CO_2 in aqueous solutions and the stability of electrode materials. In contrast, plasma catalysis represents a promising and emerging field, as it enables thermodynamically unfavorable chemical reactions to proceed under mild conditions. It offers the advantage of operation flexibility, mild reaction conditions and the potential for continuous operation.

Table S1. Summary of plasma catalysis, thermal catalysis and electrocatalysis for CO_2 hydrogenation to C_2H_5OH. (MR represents the molar ratio of H_2O to CO_2)

Plasma catalysis in this paper

Catalyst	Conditions/ Durability test	CO_2 conversion (%)	EtOH selectivity (%)	Energy consumption (kJ/mmol)
Cu_2O/CeO_2 (0 MR)	75 °C, 0.1 MPa. Durability test over 30 h.	7.3	2.1	36.9
Cu_2O/CeO_2 (0.2 MR)		7.4	6.6	26.4
Cu_2O/CeO_2 (0.5 MR)		6.4	23.2	18.7
Cu_2O/CeO_2 (1 MR)		5.8	32.5	17.6
Cu_2O/CeO_2 (1.5 MR)		5.5	45.7	14.8
Cu_2O/CeO_2 (2 MR)		4.9	55.7	15.6

Thermal catalysis (fixed bed and tank reactor)

Catalyst	Conditions	CO_2 conversion (%)	EtOH selectivity (%)	STY ($g_{EtOH}\ kg_{cat}^{-1}\ h^{-1}$)
Rh-Na/TiO_2[1]	260 °C, 1 MPa	N/A	13.3	0.2
Rh-Li/SiO_2[2]	240 °C, 5 MPa	7.0	15.5	16.6
Rh-Fe/SiO_2[3]	260 °C, 5 MPa	26.7	16.0	65.8
RhFeLi/TiO_2[4]	250 °C, 3 MPa	15.7	28.5	75.9
Fe-Rh/SiO_2[5]	250 °C, 5 MPa	18.4	16.0	N/A
Na-Rh@S-1[6]	250 °C, 5 MPa	10.0	24.0	3312.0

Li-RhY [7]	250 °C, 3 MPa	13.1	2.7	5.5
Rh-VO_x/MCM-41 [8]	250 °C, 3 MPa	12.1	24.1	47.9
Na-Co/SiO_2 [9]	300 °C, 0.5 MPa	18.8	6.0	N/A
Na–Co/SiO_2 [10]	250 °C, 5 MPa	18.8	8.7	7.4
CoMoS [11]	340 °C, 10.3 MPa	32.0	12.9	N/A
Co@Co_3O_4/C-N [12]	220 °C, 2 MPa	18.6	1.2	3.2
Na-Fe@C-CuZnAl [13]	320 °C, 5 MPa	39.2	35.0	N/A
Na-Fe_3O_4 [14]	300 °C, 0.5 MPa	30.6	38.3	N/A
IrMo-SiO_2 [15]	200 °C,4.9 MPa	12.4	5.3	N/A
Cu/Co_3O_4 [16]	250 °C, 3 MPa	13.9	15.2	86.0
* $K_{0.2}Rh_{0.2}$/b-Mo_2C [17]	150 °C, 6 MPa	N/A	72.1	N/A
* Pt/Co_3O_4 [18]	200 °C, 8 MPa	N/A	17.3	19.3
* $Ru_3(CO)_{12}/Rh_2(CO)_4Cl_2$ [19]	200 °C, 8 MPa	N/A	45.7	N/A
* CoCu [20]	200 °C, 4 MPa	N/A	61.0	460.0
* $Co_{0.52}Ni_{0.48}AlO_x$ [21]	200 °C, 4 MPa	N/A	85.7	60.4
* $CoAlO_x$ [22]	200 °C, 4 MPa	N/A	88.0	20.4
* Au/TiO_2 [23]	200 °C,6 MPa	N/A	99.0	129.7
* $CoMoC_x$ [24]	180 °C, 2 MPa	N/A	97.4	24.3
* Ir_1-In_2O_3 [25]	200 °C, 6 MPa	N/A	99.7	45.5
* Pd_2/CeO_2 [26]	240 °C, 3 MPa	9.2	99.2	2723.0
* Zr_{12}-bpdc-CuCs [27]	100 °C, 2 MPa	96	99.0	4043.4

Electrocatalysis

Catalyst/Electrocatalysts	**Durability test**	**Electrolyte**	**Electrode potential (V)**	**Faradaic efficiency (%)**
OD Cu/C [28]	3 h	0.1 M $KHCO_3$	-0.50	34.8
Cu-Cu_2O [29]	5 h	0.1 M KCl	-0.4.0	39.2
Ag-Cu_2O_{PB} [30]	3 h	0.2 M KCl	-1.20	34.0
Cu_4Zn [31]	5 h	0.1 M $KHCO_3$	-1.05	30.0
Cu_3Au [32]	3 h	0.1 M $KHCO_3$	-0.70	45.0
CuNP/N-doped CNS [33]	1 h	0.1 M $KHCO_3$	-1.20	63.0
CuNP/N-doped GO [34]	N/A	0.1 M $KHCO_3$	-0.25	56.3
Cu/C-0.4 [35]	1 h	0.1 M $KHCO_3$	-0.70	91.0
FeTPP/Cu [36]	N/A	0.1 M $KHCO_3$	-0.82	41.2
RuPC/NPC [37]	3 h	0.5 M $KHCO_3$	-1.07	38.4

Temperature distribution measured by infrared camera

We measured the temperature distribution of the DBD reactor using an infrared camera at different radial positions, in top view, when the plasma was turned on. As shown in Figure S1, the temperature at the catalyst bed boundary (61.5 °C) is close to the temperature of the circulating water (59.8 °C), while the center of the catalyst bed exhibits a higher temperature of around 75 °C.

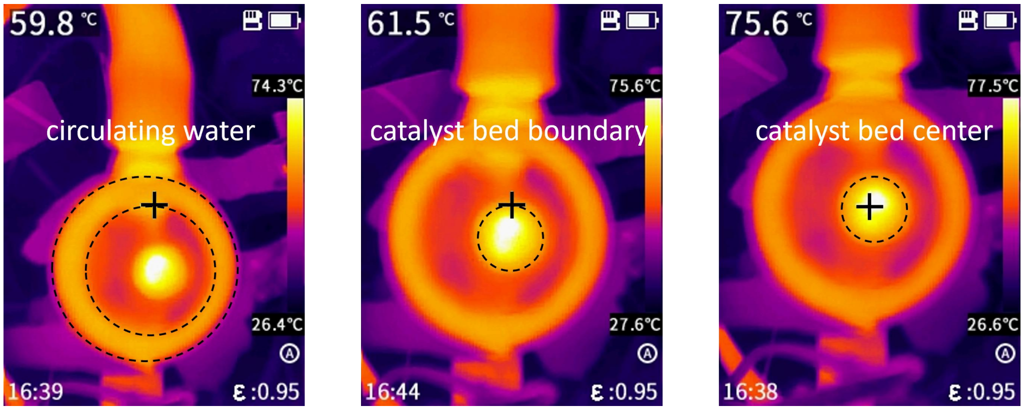

Figure S1 Temperature distribution of the DBD reactor obtained by an infrared camera. The dashed lines delineate the boundary of the reactor, and the intersecting crosses represent the points for the temperature measurements.

Performance of different Cu-based catalysts without H_2O addition

When Cu_2O is supported on various materials denoted as X (where X = Al_2O_3, SiO_2, Fe_2O_3 or CeO_2), the CH_3OH selectivity falls within the range of 30-40%. In contrast, the use of TiO_2 and ZrO_2 supports results in significantly lower CH_3OH selectivity and reduced CO_2 conversion efficiency. Notably, trace amounts of C_2H_5OH (selectivity 2.1%) were detected in the Cu_2O/CeO_2 product, a phenomenon absent when employing alternative support materials.

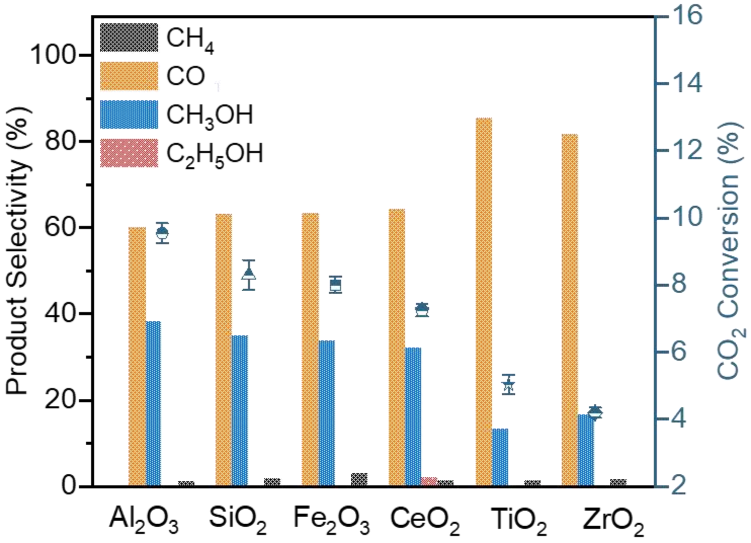

Figure S2 Product selectivity and CO_2 conversion with Cu-based catalysts (5 wt.% loading) on different support materials in plasma-catalytic CO_2 hydrogenation without H_2O addition. (CO_2/H_2 = 1/3, input power 23 W, discharge frequency 9.5 kHz, 75 °C)

Influence of discharge power and H_2/CO_2 molar ratio without H_2O addition

Enhanced CO_2 conversion is achieved under high power conditions, primarily attributed to the higher density of energetic electrons, promoting the dissociation of CO_2. Nonetheless, this condition also accelerates the reverse water-gas-shift (RWGS) reaction, leading to a heightened CO production rate. Significantly, as the H_2/CO_2 molar ratio increased from 1 to 3, the CO_2 conversion increased from 6.3% to 7.3% and the alcohols selectivity rose from 24.8% to 34.2%. In this work, we employed a critical input power of ca. 23 W for the plasma reaction, representing the minimal power threshold for sustaining discharge, with the H_2/CO_2 molar ratio set at 3.

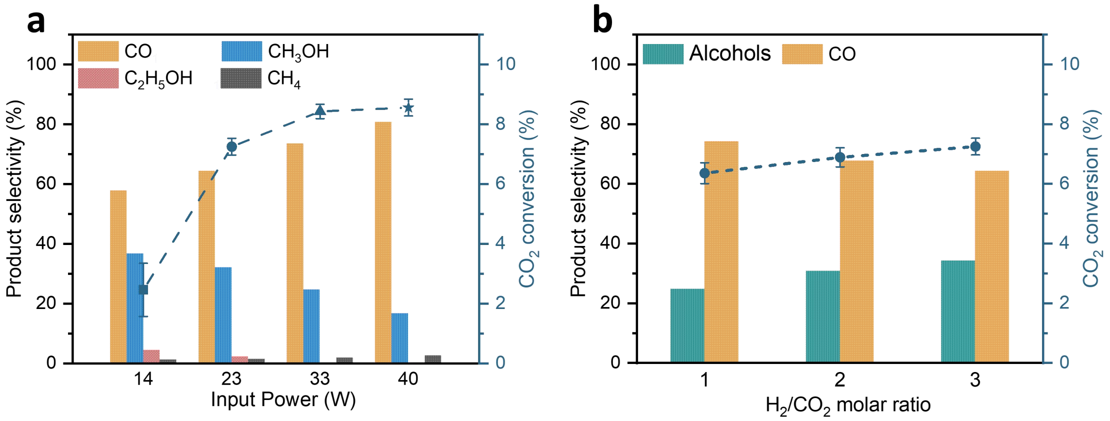

Figure S3 Influence of (a) discharge power and (b) H_2/CO_2 molar ratio on product selectivity and CO_2 conversion in the CO_2/H_2 plasma. (CO_2/H_2 = 1/3, input power 23 W, discharge frequency 9.5 kHz, 75 °C)

Influence of circulating water temperature and Cu loading without H_2O addition

The optimized temperature for CO_2 hydrogenation to produce alcohols in a water electrode DBD reactor is ~60 ºC. At this temperature, the average temperature at the rear end of the discharge area is ~75 ºC (Figure S1). Consequently, the temperature at the midpoint of the discharge zone is slightly above the boiling point of C_2H_5OH (78.4 ºC) and exceeds the boiling point of CH_3OH (64.8 ºC). However, a lower circulating water temperature (20 ºC and 40 ºC) may inhibit alcohols desorption, while a higher circulating water temperature (80 ºC) may promote the RWGS reaction. Furthermore, both CO_2 conversion and alcohols selectivity exhibit a volcano curve with increasing Cu loading. The optimal alcohols yield was achieved at a 5 wt.% loading, indicating that a modest loading is beneficial for plasma-catalytic CO_2 hydrogenation to alcohols.

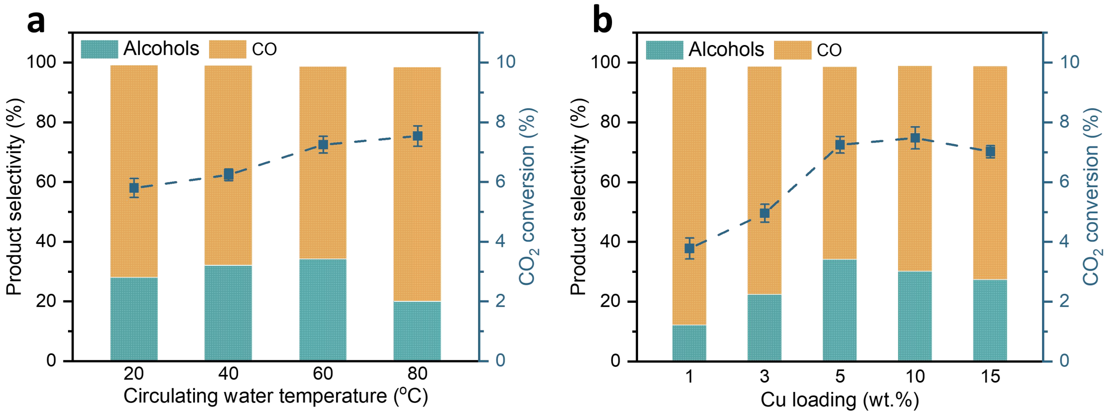

Figure S4 Influence of (a) circulating water temperature and (b) Cu loading on product selectivity and CO_2 conversion in the CO_2/H_2 plasma. ($CO_2/H_2 = 1/3$, input power 23 W, discharge frequency 9.5 kHz, 75 °C)

Waveforms of discharge voltage and current

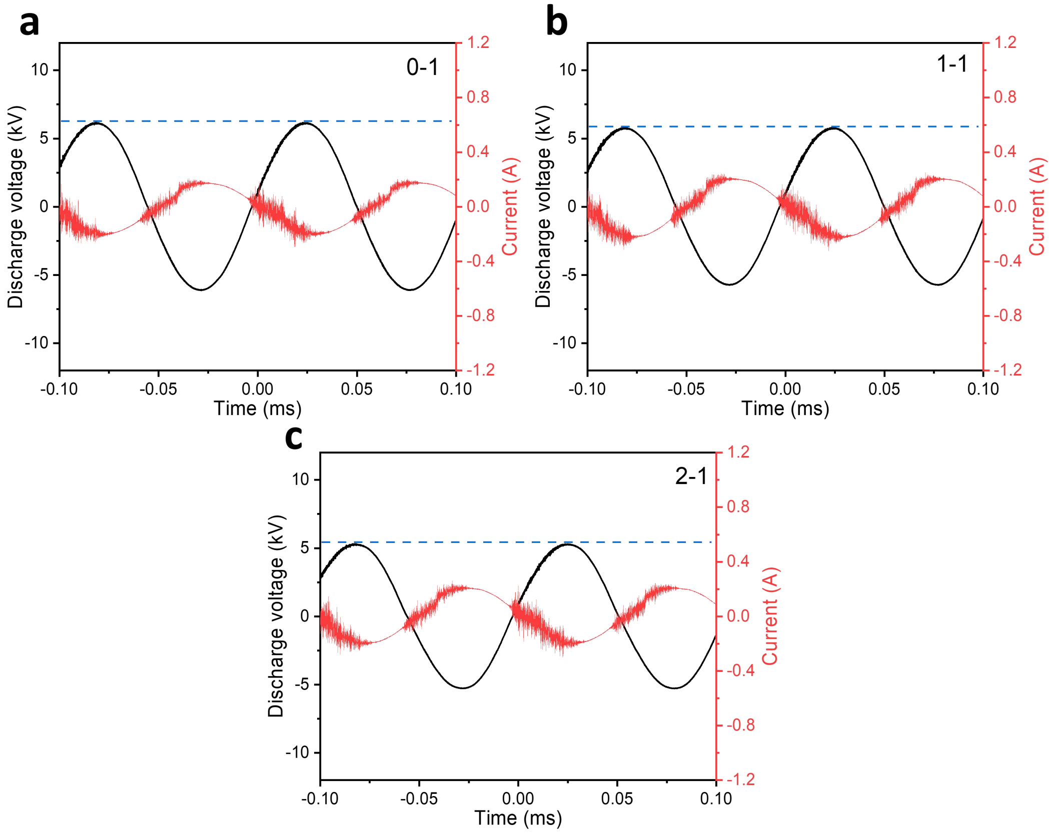

Figure S5 Waveforms of discharge voltage and current with varying H_2O/CO_2 molar ratios, indicating a slight drop in discharge voltage upon higher water content. (a) 0-1; (b) 1.5-1; (c) 2-1.

Normalized production rates of reaction products over Cu_2O/CuO catalysts

Table S2 Normalized production rates of reaction products over Cu_2O/CuO catalysts with varying H_2O/CO_2 molar ratios.

Samples	CO ($\mu mol \cdot g^{-1} \cdot h^{-1}$)	CH_3OH ($\mu mol \cdot g^{-1} \cdot h^{-1}$)	C_2H_5OH ($\mu mol \cdot g^{-1} \cdot h^{-1}$)	CH_4 ($\mu mol \cdot g^{-1} \cdot h^{-1}$)
Cu_2O-CeO_2 (0-1)	1024.7	510.2	33.5	20.5
Cu_2O-CeO_2 (0.2-1)	907.6	593.4	107.0	20.4
Cu_2O-CeO_2 (0.5-1)	581.6	484.3	326.4	16.9
Cu_2O-CeO_2 (1-1)	461.1	384.7	413.8	13.8
Cu_2O-CeO_2 (1.5-1)	299.3	347.2	553.5	11.9
Cu_2O-CeO_2 (2-1)	218.6	232.0	578.3	10.0

Results of qualitative analysis

Figures S6a and S6b present the gas chromatography data for the feed gas and exhaust gas, with the use of 2% N_2 as an internal reference to ensure precise quantification of the CO content. Notably, the FID detected only trace amounts of CH_4, with concentrations below 0.04%. For the measurements of liquid products, signal values under conditions 1-1 and 2-1 were amplified by factors of 10 and 50, respectively, to compensate for the dilution effect caused by water. (Figures S6 c-d)

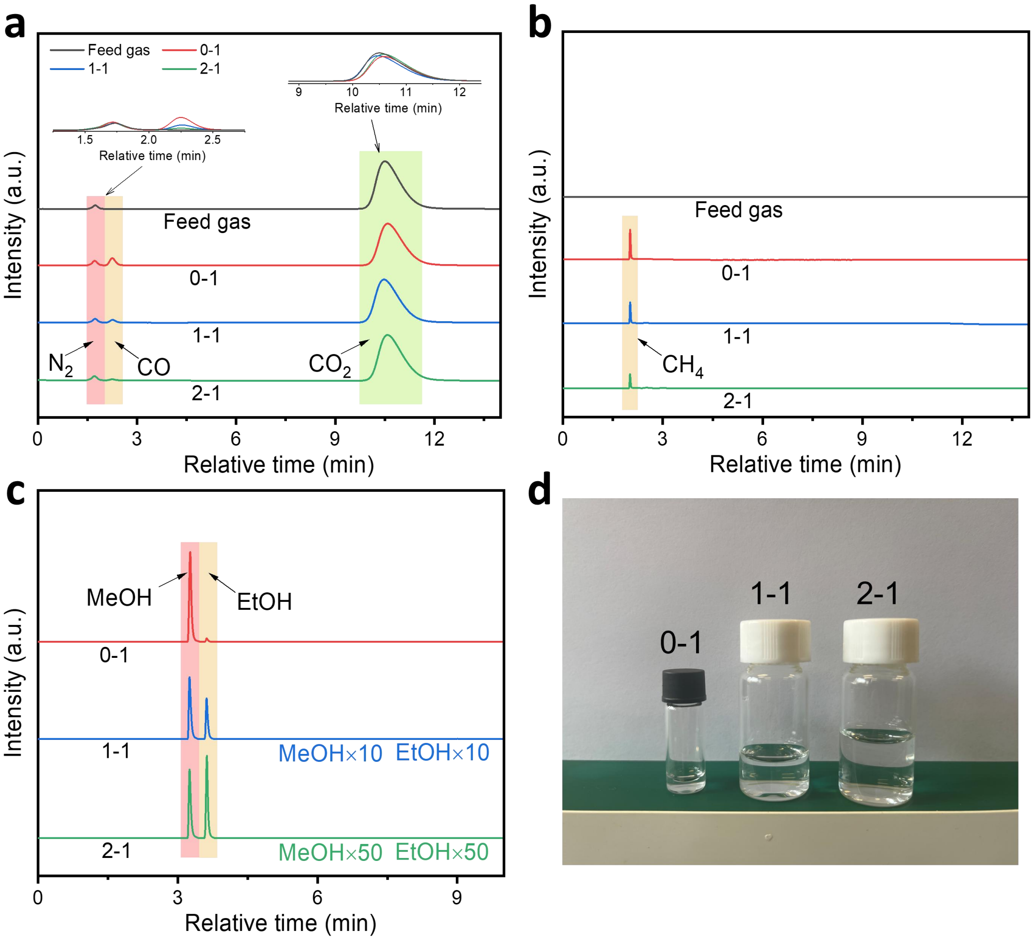

Figure S6 (a) Chromatographic profiles of the feed gas and exhaust gas at different H_2O/CO_2 ratios after reaction obtained by TCD; (b) Chromatographic profiles of the feed gas and exhaust gas at different H_2O/CO_2 ratios after reaction obtained by FID; (c) Chromatographic profiles of the liquid products at different H_2O/CO_2 ratios after reaction obtained by FID; (d) Comparison of liquid product volumes.

Carbon balance calculations with varying H_2O/CO_2 molar ratios

As shown in Figure S7a, the presence of liquid residues on quartz wool and the collector walls results in a collected liquid volume smaller than the actual liquid product, which becomes more pronounced when the total collected liquid is small. Achieving a 100% carbon balance, particularly within the initial 8 hours, proves to be challenging when water is not added (calculated using Eq. 5 and 6) (Figure S7b). However, as the reaction time becomes sufficiently long, the proportion of carbon "loss" caused by liquid residues decreases. Therefore, we performed reaction performance calculations in the absence of water using Eq. (4). (The fit of the standard curves for CO_2, CO and CH_4 in the gas chromatogram is greater than 99.9%).

The liquefaction of products cannot be overlooked, especially with a high-water content, which will have an impact on the measurement of gas velocity and may pose a challenge to the accuracy of the data. Two strategies can contribute to addressing this issue: (i) extending the length of the exhaust pipe and (ii) augmenting the frequency of gas velocity measurements and subsequently obtaining the average. With increasing water content, the calculated molar yield of the products, i.e., n($CO+CH_4+CH_3OH+C_2H_5OH$), will exceed the molar change of CO_2 detected by gas chromatography, resulting in a carbon balance exceeding 100%. This may be attributed to the instability of gas velocity. (Figures S7 c-d)

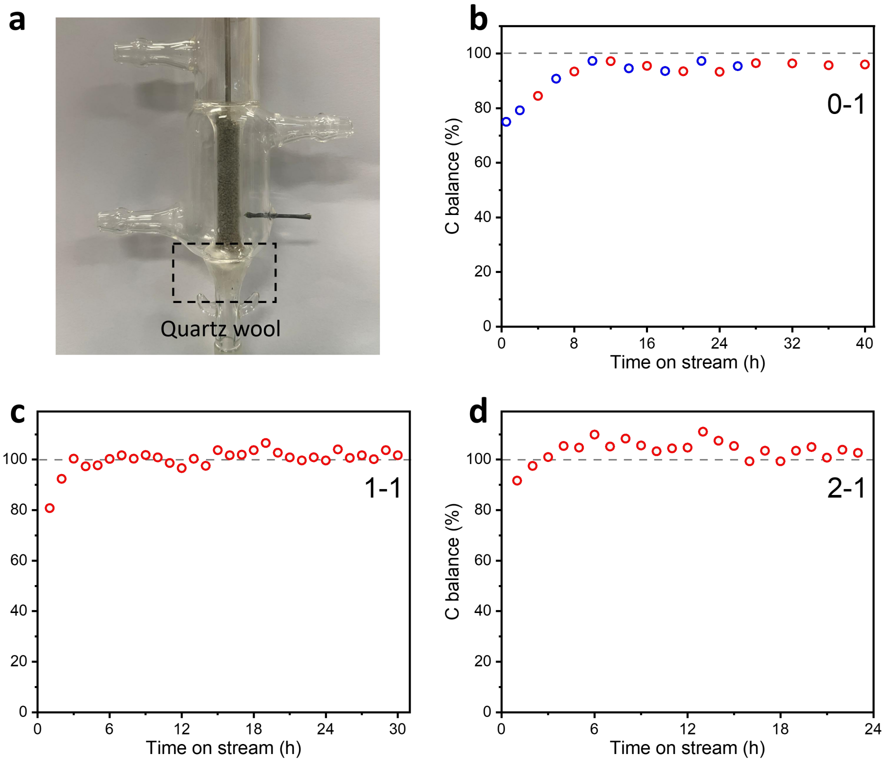

Figure S7 (a) Image of the water electrode reactor (with the catalyst supported by quartz wool); (b-d) Carbon balance calculations with varying H_2O/CO_2 molar ratios. (The blue circles represent repetitive experiments, with only the sampling time being modified)

Stability testing of catalysts with varying H_2O/CO_2 molar ratios

The stability of the catalyst is observed to be excellent when the H_2O/CO_2 molar ratio is maintained within the range of 0 to 1.5. During 30 hours of continuous operation, a slight reduction in CO_2 conversion is observed. However, when the H_2O/CO_2 molar ratio reaches 2, an accumulation of water on the catalyst surface results in a decrease in the overall dielectric constant of the packing material, leading to the suppression of filamentary discharge. To overcome this, it is necessary to cease the supply of feed gases and switch to Ar as the purge gas. Maintaining this condition for 10 minutes at an input power of 40 W allows the discharge system to return to a stable state.

In addition, it should be noted that the superior stability of the MS signal compared to that of the stability testing results from the intermittent injection of H_2O (H_2O is rapidly consumed within minutes).

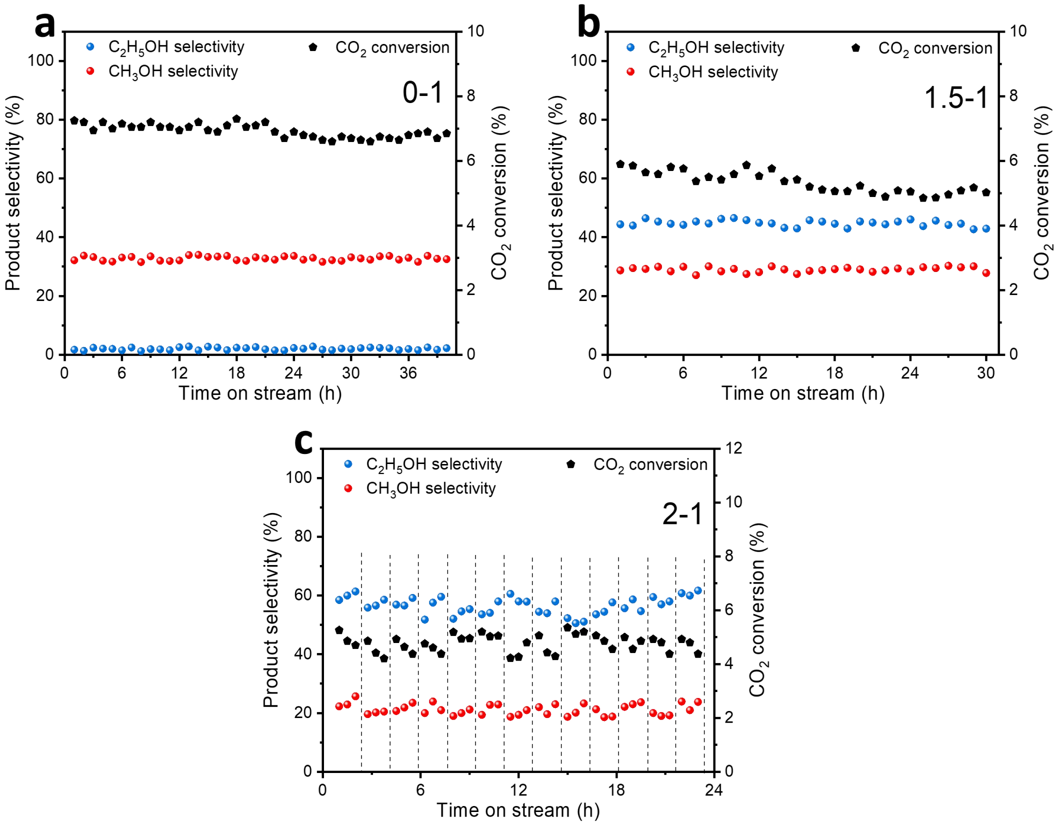

Figure S8 Stability testing of catalysts with varying H_2O/CO_2 molar ratios. (a) 0-1; (b) 1.5-1; (c) 2-1.

Performance on different supports with varying H_2O/CO_2 molar ratios

Figure S9 shows the product selectivity and CO_2 conversion of Cu-based catalysts on different supports with varying H_2O/CO_2 molar ratios. The C-C coupling will not occur when a low content of water was employed for plasma-catalytic CO_2 hydrogenation over the Cu_2O/Al_2O_3, Cu_2O/SiO_2 and Cu_2O/Fe_2O_3 catalysts, and C_2H_5OH will only appear when water reaches a certain content. A similar investigation was conducted for Cu_2O/TiO_2 and Cu_2O/ZrO_2; however, the exceedingly low CO_2 conversion led to the production of alcohols falling below the detection threshold.

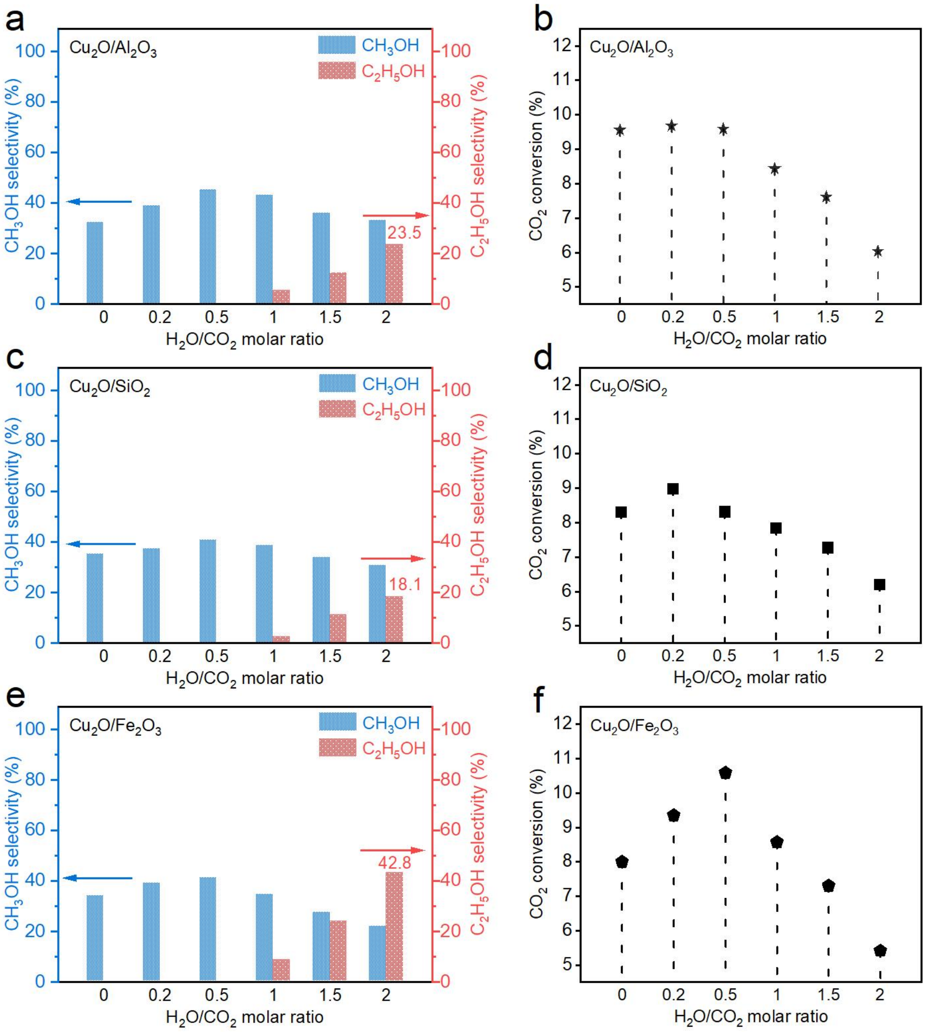

Figure S9 Product selectivity and CO_2 conversion of Cu-based catalysts on different supports with varying H_2O/CO_2 molar ratios. (a, b) Cu_2O/Al_2O_3; (c, d) Cu_2O/SiO_2; (e, f) Cu_2O/Fe_2O_3. (CO_2/H_2 = 1/3, input power 23 W, discharge frequency 9.5 kHz, 75 °C)

CO selectivity on different supports with varying H_2O/CO_2 molar ratios

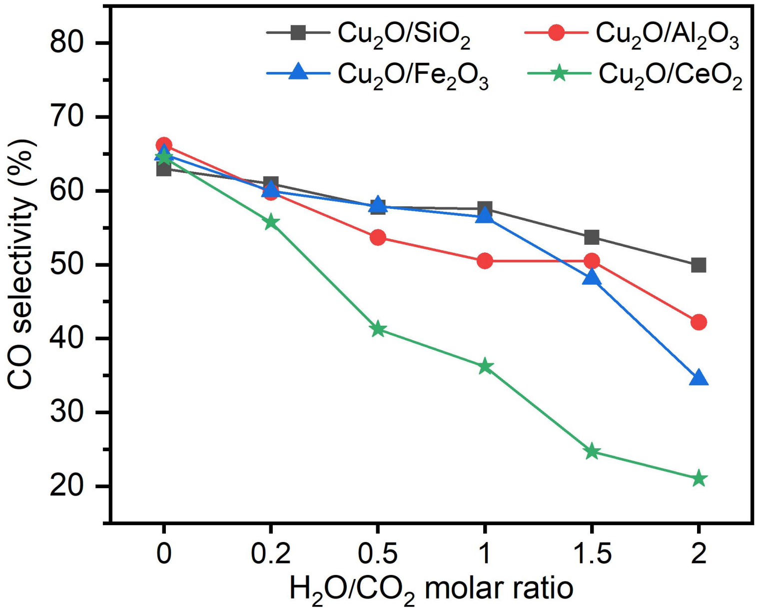

Figure S10 CO selectivity of Cu-based catalysts on different supports with varying H_2O/CO_2 molar ratios. (CO_2/H_2 = 1/3, input power 23 W, discharge frequency 9.5 kHz, 75 °C)

Performance with different feedstocks

The H_2O dissociation is more difficult at low power and a small amount of H from the dissociation of H_2O could not hydrogenate CO_2 into alcohols, as is clear from Figure S11.

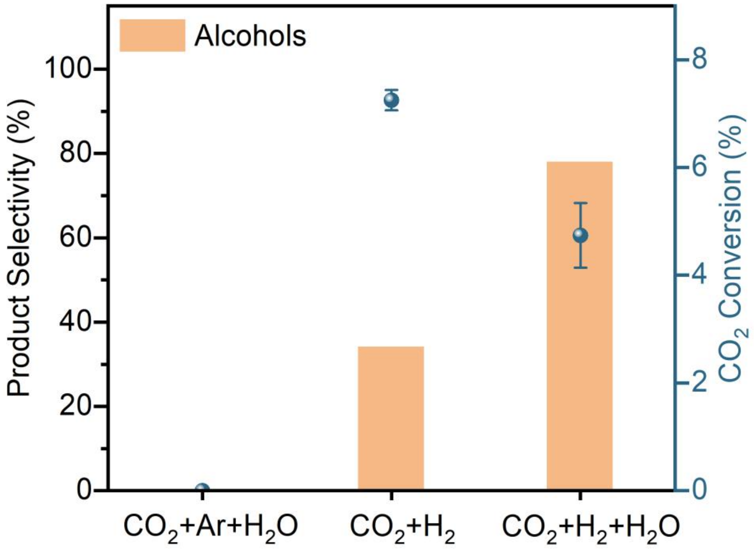

Figure S11 Alcohols selectivity and CO_2 conversion of Cu_2O/CeO_2 catalysts with different feedstocks. (Input power 23 W, discharge frequency 9.5 kHz, 75 °C, $CO_2/H_2O/Ar$ = 1/2/3, H_2/CO_2 = 3/1 and $H_2/CO_2/H_2O$ = 3/1/2)

CO_2 conversion with different reaction systems

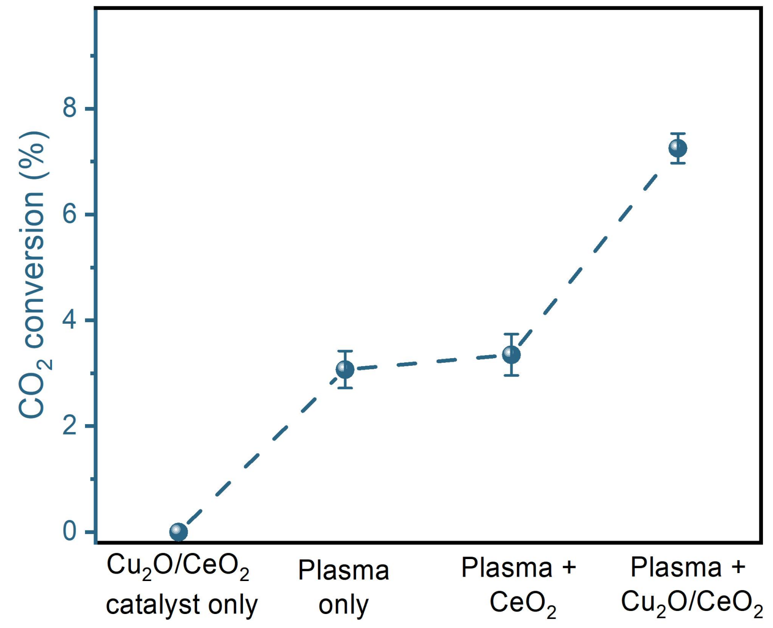

Figure S12 CO_2 conversion for catalysis-only, plasma-only, plasma catalysis with CeO_2 and 5 wt.% Cu_2O/CeO_2. (CO_2/H_2 = 1/3, input power 23 W, discharge frequency 9.5 kHz, 75 °C)

Energy consumption in different configurations (plasma-only, packing with CeO_2 and with Cu_2O/Ce_2O catalyst) without and with different H_2O contents

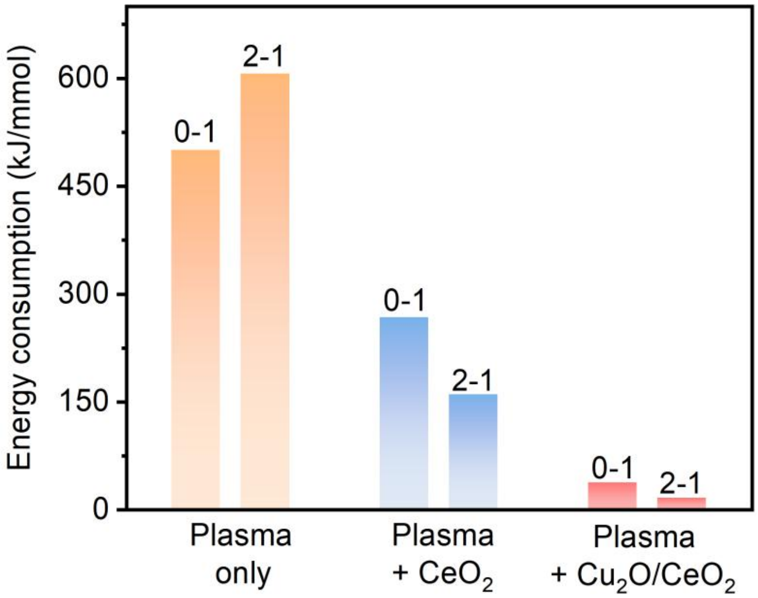

Figure S13 Energy consumption of plasma-only and plasma with CeO_2 support or with Cu_2O/CeO_2 catalyst, without and with different H_2O contents. (0-1 and 2-1 represent the different H_2O/CO_2 molar ratios)

Electron energy distribution function

The EEDF is calculated by Bolsig+. As input, we used a discharge gap of 3 mm and a simplified packing fraction of both the CeO_2 support and the Cu_2O/CeO_2 catalyst of 0.8. The dielectric constants of CeO_2 and Cu_2O/CeO_2 are 7.2 and 7.9, respectively. In the Bolsig+ input, the discharge frequency is 9.5 kHz (which corresponds to an angular frequency of 2.91×10^{-19} $m^3\cdot rad/s$), while the voltage amplitude for the three systems (non-packed, CeO_2 and Cu_2O/CeO_2) is averaged after three times sampling. All the cross-section data are read from the Morgan database in www.lxcat.net. Both Figure 2 and Figure S14 indicate that the packed systems show much higher E/N, which mostly accounts for the generation of high-energy electrons in the plasma-catalyst systems.

During the calculation, attachment, elastic, ionization and excitation reactions are considered for both the CO_2/H_2 and $CO_2/H_2/H_2O$ systems to calculate their EEDF. Due to the complexity of the DBD filament discharge, we use the average E/N rather than its undetectable maximum value to conduct the zero-dimensional (0D) Bolsig+ simulation and is to qualitatively address the effect of catalyst packing on plasma reactive species from a global perspective.

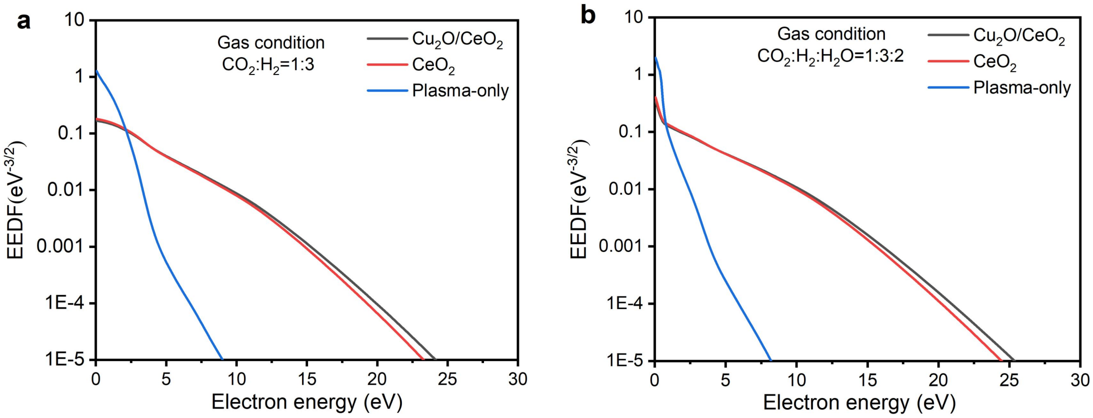

Figure S14 Electron energy distribution function (EEDF), for plasma-only and plasma with CeO_2 support or with Cu_2O/CeO_2 catalyst, and for two different plasma compositions.

OES results for different H_2O/CO_2 molar ratios

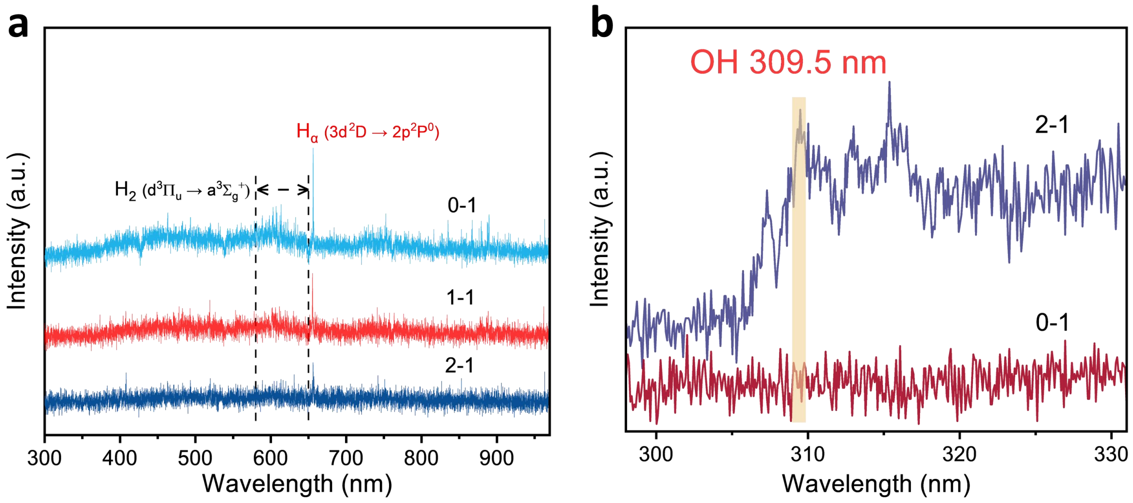

Figure S15 OES results for different H_2O/CO_2 molar ratios. (a) Catalyst packing plasma conditions; (b) plasma only. (0-1, 1-1 and 2-1 represent the H_2O/CO_2 molar ratio)

HAADF-STEM images and EDX elemental maps

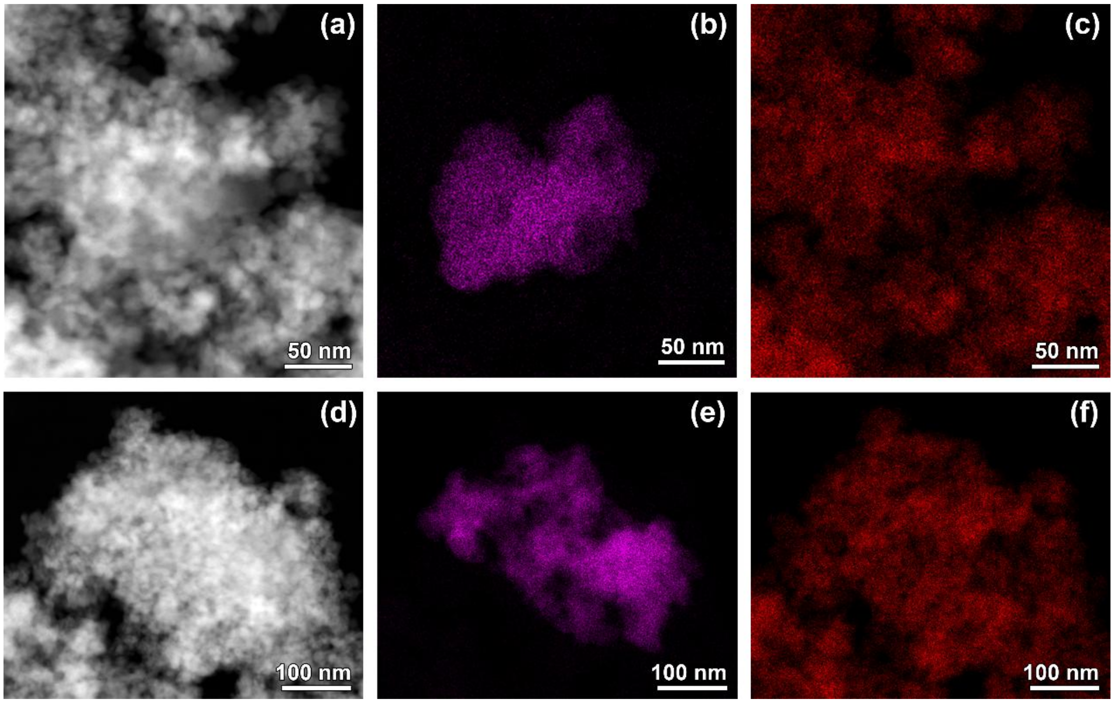

Figure S16 (a), (d) HAADF-STEM images of spent Cu_2O/CeO_2 catalyst and corresponding EDX elemental maps: (b), (e) Cu, (c), (f) Ce.

Average particle size and size distribution of CuO

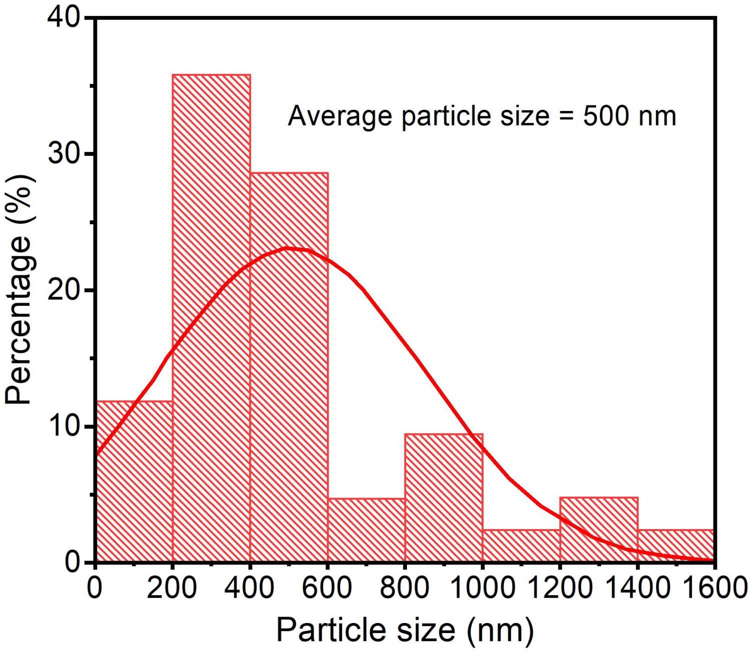

Figure S17 The average particle size and particle size distribution of copper in the Cu_2O/CeO_2 catalyst obtained from EDX elemental maps.

XPS fitting information

Curve fitting was conducted using XPS Peak software, with the C1s calibration set to 284.8 eV. In this study, the residual values for Cat-F and Cat-S (2-1) were determined as 4.67 and 1.63, respectively. Additionally, the peak area ratio of Cu $2p_{3/2}$ to Cu $2p_{1/2}$ was approximately 2.

Table S3 XPS fitting information for Cat-F and Cat-S (2-1) samples.

Cat-F						
Binding energy	—	934	942.9	—	953.8	962.8
FWHM	—	2.95	—	—	3.07	—
Area	—	31644	—	—	15346	—
Cat-S (2-1)						
Binding energy	932.9	934	942.9	952.8	953.8	—
FWHM	1.87	2.62	—	2.26	2.49	—
Area	19750	8910	—	10179	4301	—

Cu 2p XPS result with Ar$^+$ etching

The Cu 2p XPS result shows only Cu$^+$ species, which means that the thickness of the Cu_2O layer on the catalyst surface is more than 10 nm.

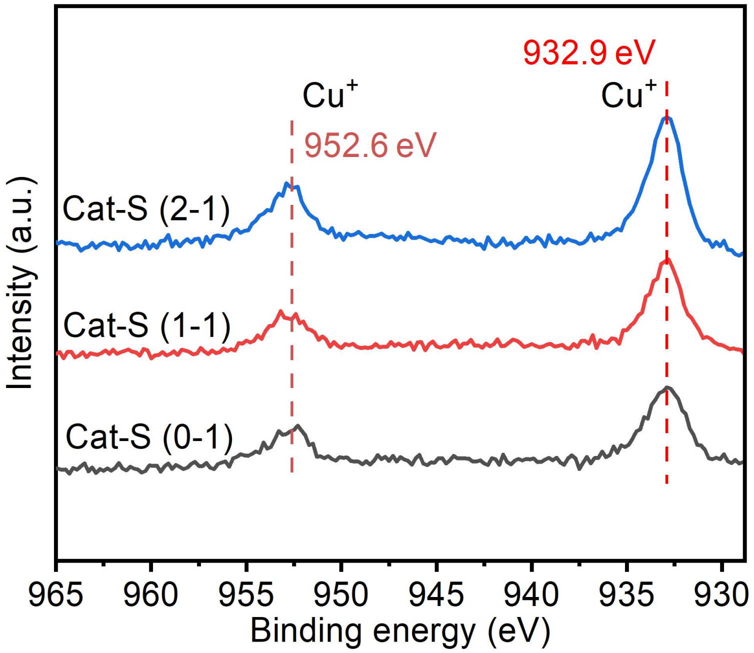

Figure S18 Cu 2p XPS result with Ar$^+$ etching (etching time: 60 s; etching depth: 10 nm).

Cu LMM Auger spectra of Cat-HF and Cat-HS (2-1)

The Cu LMM Auger spectra show that the Cu^0 species of the fresh catalyst (Cat-HF) are oxidized to Cu^+ species after plasma. The fresh catalyst reduced by H_2 plasma (30 mL/min H_2, 300 °C) is denoted as Cat-HF, and the spent catalyst in the same way is denoted as Cat-HS.

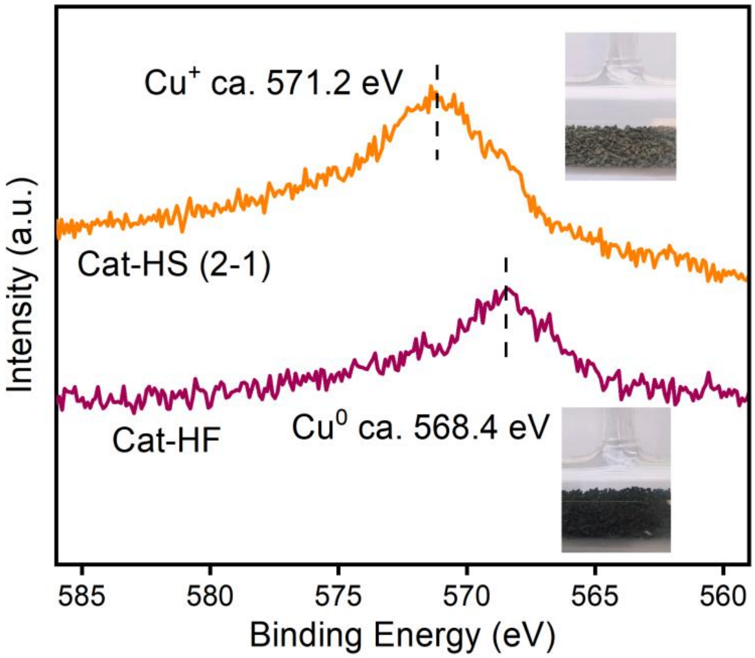

Figure S19 Cu LMM Auger spectra of Cat-HF and Cat-HS (2-1) with digital photograph.

N_2 adsorption isotherms and pore size distribution

The isotherm adsorption of the fresh Cu_2O/CeO_2 catalyst was slightly increased compared to the bare support CeO_2, while the hysteresis and the shape of the isotherm are well retained. The isotherms of the Cu_2O/CeO_2 samples are characteristic of type IV, indicating that the samples are mesoporous, which may be attributed to stacking of the grains. The BET surface area had a slight decrease for the catalysts after loading with metal, which can be attributed to the impregnation of the precursor in the support pores, and the spent catalysts showed isotherms similar to the fresh catalyst.

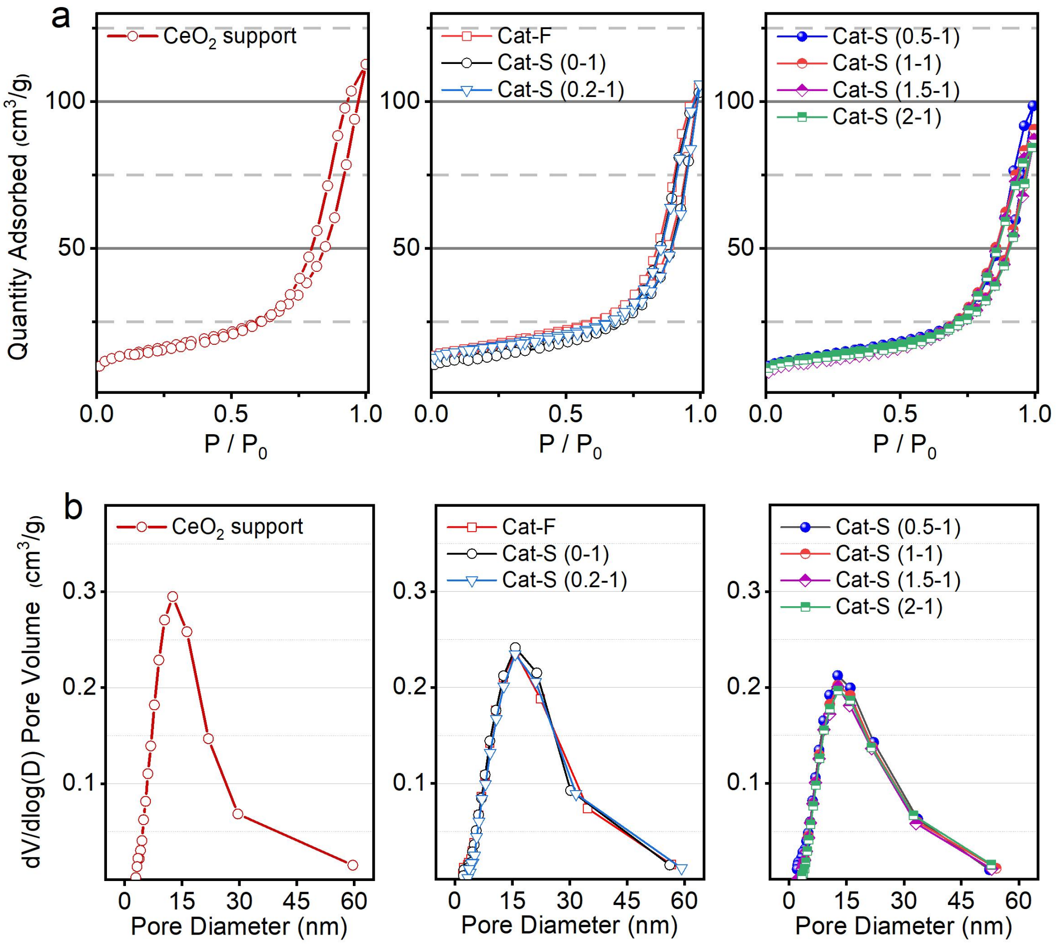

Figure S20 (a) N_2 adsorption isotherms and (b) pore size distribution for CeO_2 support, fresh and spent Cu_2O/CeO_2 catalysts.

N_2 physisorption data with different H_2O content

Table S4 N_2 physisorption data with different H_2O content.

Samples	S_{BET} (m^2 g^{-1})	V_{total} (cm^3 g^{-1})	Pore diameter (nm)
CeO_2 support	53.9	0.17	12.7
Cat-F	48.5	0.16	13.0
Cat-S (0-1)	48.1	0.16	13.2
Cat-S (0.2-1)	46.2	0.16	13.7
Cat-S (0.5-1)	45.4	0.15	12.8
Cat-S (1-1)	44.6	0.14	12.6
Cat-S (1.5-1)	44.3	0.13	11.5
Cat-S (2-1)	43.4	0.13	12.4

Characterization of spent Cu_2O/CeO_2 catalysts with different H_2O content

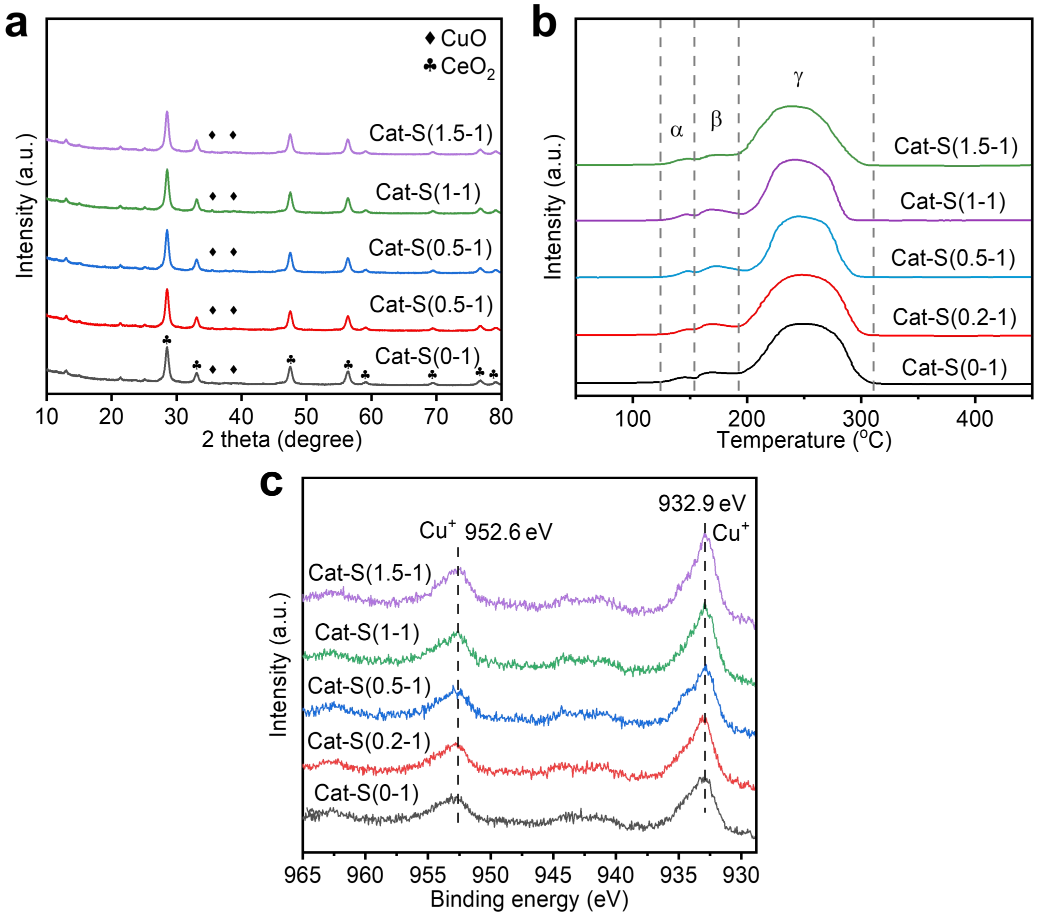

Figure S21 Characterization of spent Cu_2O/CeO_2 catalysts with different H_2O content: (a) PXRD; (b) TPR; (c) Cu 2p XPS results.

GC-MS spectra of isotope-tracing experiments

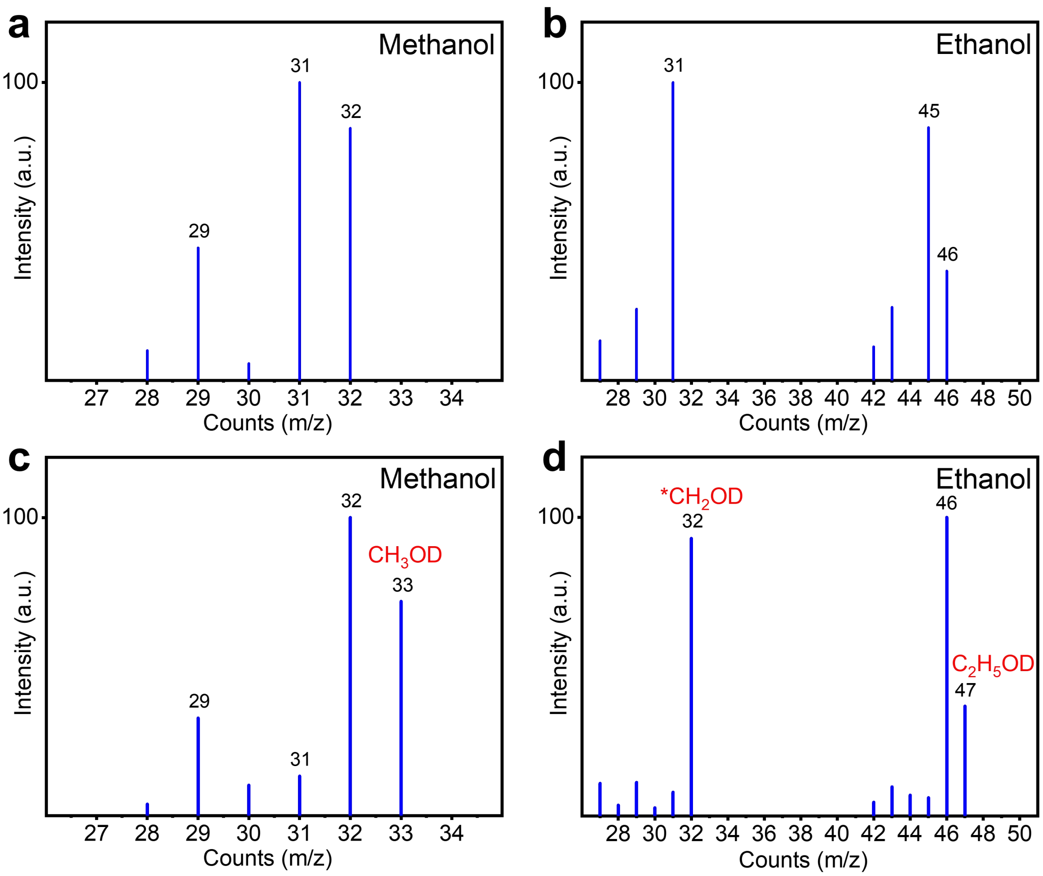

Figure S22 GC-MS spectra of isotope-tracing experiments in CO_2 hydrogenation over Cu_2O/CeO_2 catalyst. (a, b) CO_2 hydrogenation with H_2O under plasma condition; and (c, d) upon addition of 0.5% CH_3OH and 0.5% C_2H_5OH to the solvent with a physical mixture (99% H_2O, 1% D_2O).

H_2/D_2O experiment ruslts

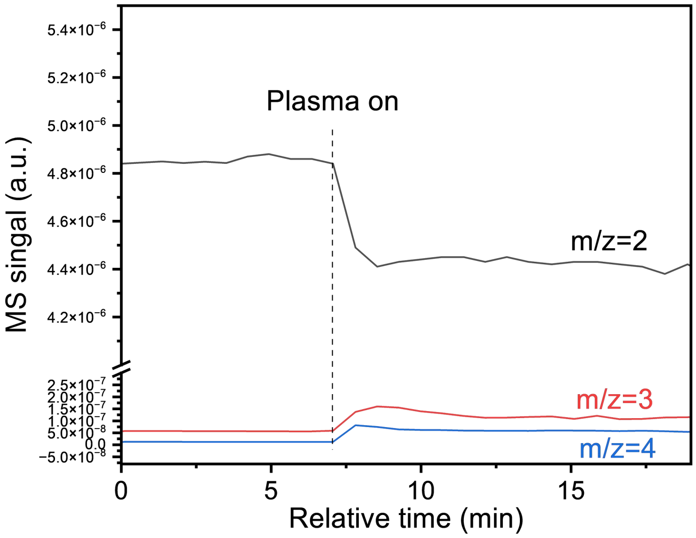

Figure S23. Mass spectrometry signals of m/z = 3 (HD) and m/z = 4 (D_2) in the H_2/D_2O system.

EPR results of the liquid products

5,5-Dimethyl-1-pyrroline N-oxide (DMPO) was used to trap OH radicals in the reaction system.

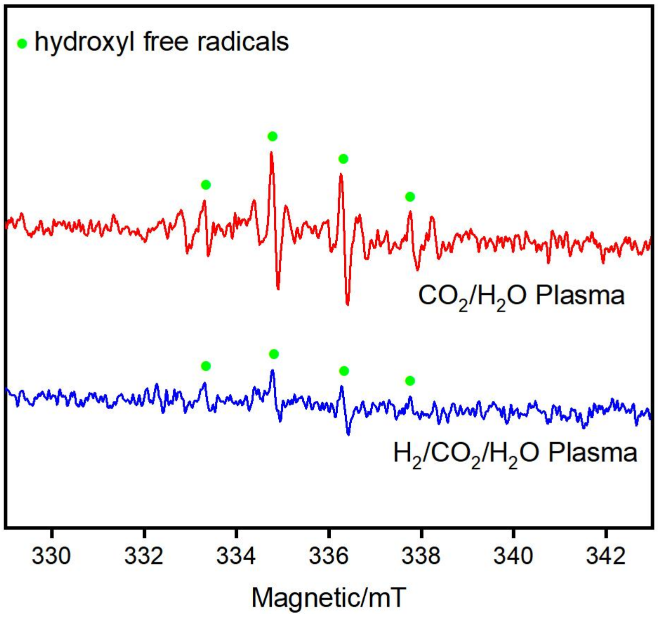

Figure S24 EPR spectra of the liquid products in both CO_2/H_2O and $H_2/CO_2/H_2O$ plasma.

Ideal Cu_2O (111) surface

Catalyst characterization reveals that approximately 90% of the Cu species exist in the form of bulk Cu oxides phases. Consequently, the selection of a DFT model emphasizes the predominant Cu_2O phase, rather than highly dispersed CuO and Cu-O_x-Ce solid solution.

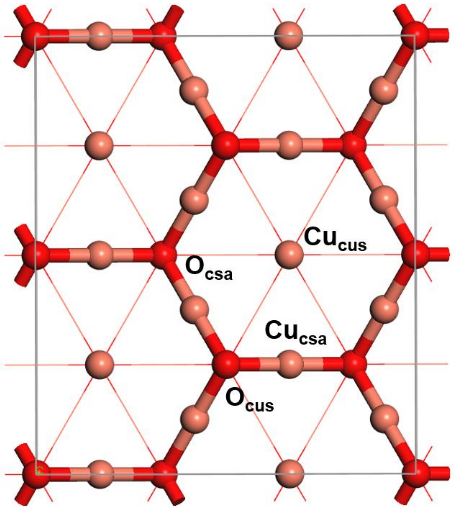

Figure S25 Ideal 2×2 Cu_2O (111) surface (unrelaxed). The surface layer is shown in ball and stick format, Cu_{cus} and Cu_{csa} are the coordinatively unsaturated and saturated surface Cu atoms. Copper and oxygen atoms are colored copper and red, respectively.

Adsorption energy of gas species and intermediates at typical sites

Table S5 Adsorption energy (eV) of the main gases and intermediates at typical sites over the Cu_2O (111) surface.

	Cu_{cus}	Cu_{csa}	O_{cus}	O_{cas}
CO_2	-0.29	-0.27	-0.21	-0.23
H_2	-0.40	-0.12	-0.11	-0.09
CO	-1.97	-0.75	-0.70	-0.75
HCO	-2.04	-0.95	-2.00	-1.76
H_2CO	-0.79	-0.33	-0.34	-0.40
OH	-2.58	-2.63	-2.55	-2.66
H_2O	-0.94	-0.78	-0.38	-0.27

Adsorption configurations of main gases and intermediates

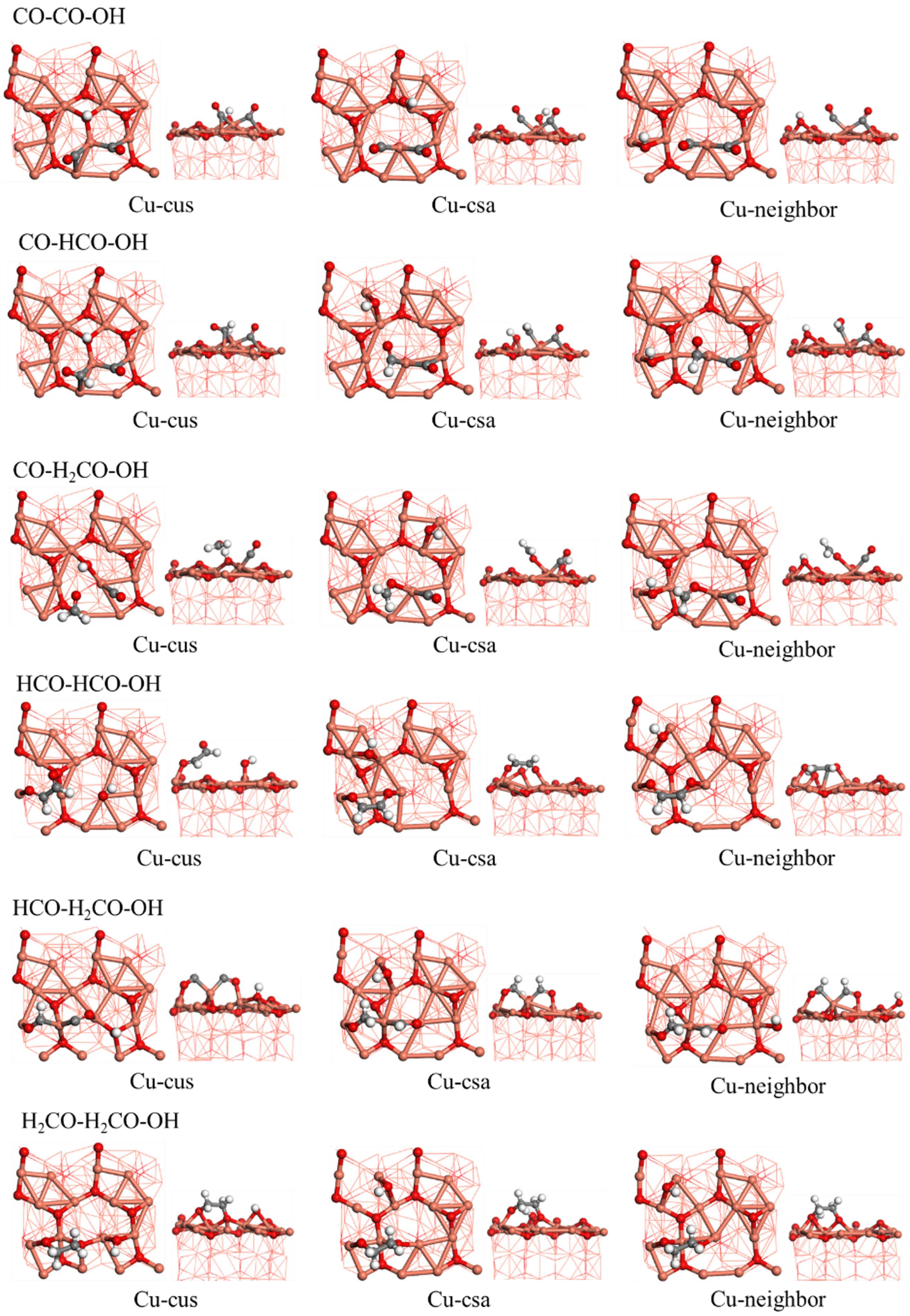

Figure S26 Adsorption configurations of main gases and intermediates over Cu_2O (111) surface.

Formation of CH_3O^* and CH_3^* by CH_3OH^* bond breaking

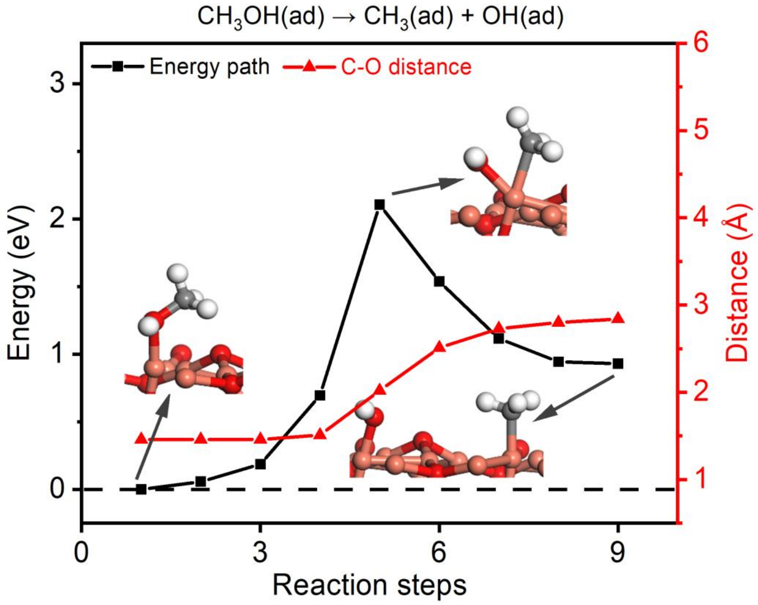

Figure S27 Formation of CH_3^* by CH_3OH^* bond breaking.

Formation of CH_3CO^* and CH_4^*

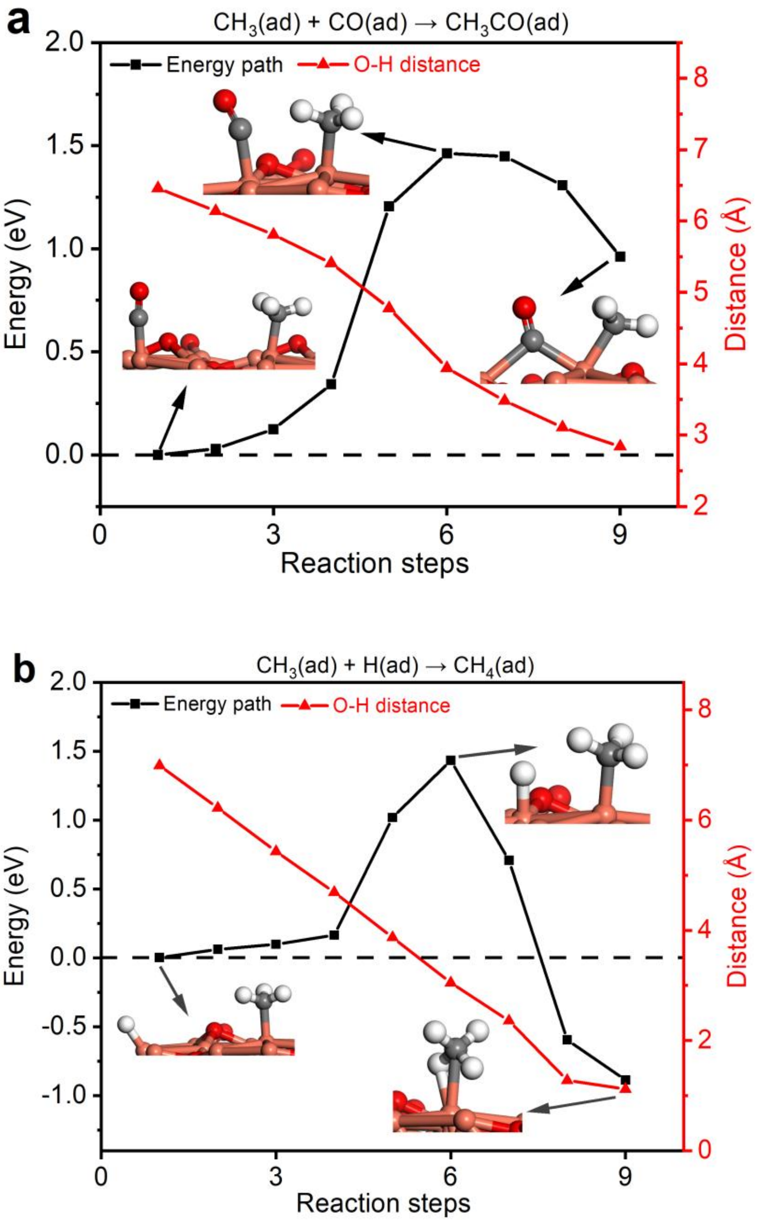

Figure S28 (a) CH_3CO^* formation from CH_3^* and CO^*; (b) CH_4^* formation from CH_3^* and H^*.

Reaction energy and activation barrier for C-C coupling

Table S6 Reaction energy and activation barrier at 0 K for C-C coupling.

C-C coupling pair	ΔE(eV)	E_a(eV)
$CO^* + CH_3^* \rightarrow OCCH_3^*$	0.96	1.46
$CO^* + CO^* \rightarrow OCCO^*$	0.92	1.51
$CO^* + CHO^* \rightarrow OCCHO^*$	0.99	1.40
$CO^* + CH_2O^* \rightarrow OCCH_2O^*$	0.71	0.91
(OH pre- adsorbed) $CO^* + CH_2O^* \rightarrow OCCH_2O^*$	0.66	0.85
$CHO^* + CHO^* \rightarrow OHCCHO^*$	0.46	1.32
(OH pre-adsorbed) $CHO^* + CHO^* \rightarrow OHCCHO^*$	-0.38	1.56
$CHO^* + CH_2O^* \rightarrow OHCCH_2O^*$	0.65	1.24
$CH_2O^* + CH_2O^* \rightarrow OH_2CCH_2O^*$	0.15	1.21

C-C coupling TS states and their coordinates

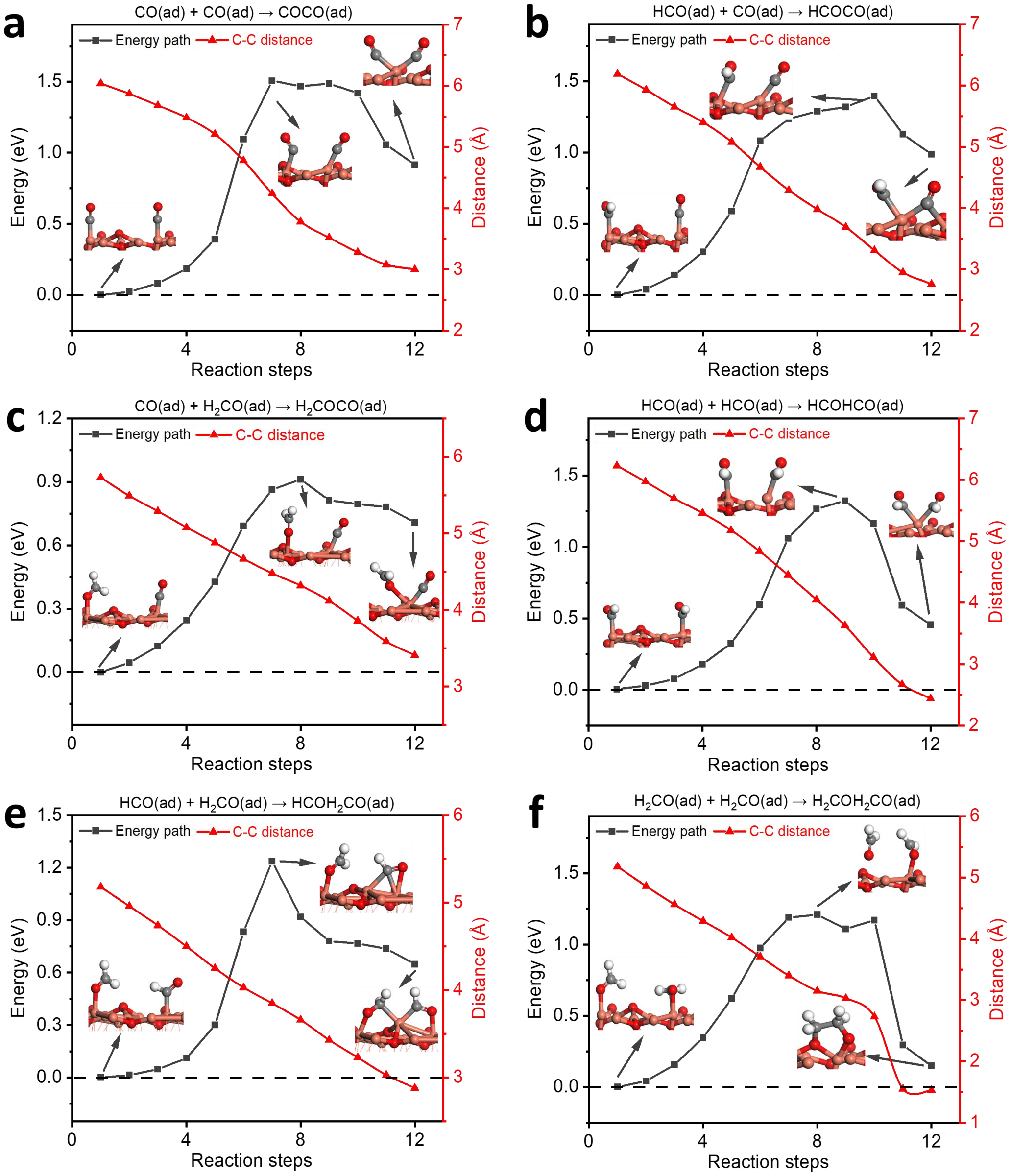

Figure S29 C-C coupling at the Cu_{cus} sites on the surface of Cu_2O (111). (a) CO*-CO*; (b) HCO*-CO*; (c) H_2CO*-CO*; (d) HCO*-HCO*; (e) HCO*-H_2CO* and (f) H_2CO*-H_2CO*.

Adsorption energy of possible C-C coupling species

Table S7 Adsorption energy (eV) of possible C-C coupling species at typical sites over the Cu_2O (111) surface.

	Cu_{cus}	Cu_{csa}	O_{cus}	O_{cas}
CO-CO	-3.23	-3.89	-3.01	-3.90
CO-HCO	-3.02	-4.00	-3.21	-2.29
CO-H_2CO	-2.14	-2.83	-1.17	-2.87
HCO-HCO	-3.58	-3.30	-2.93	-3.47
HCO-H_2CO	-2.02	-2.22	-4.30	-2.27
H_2CO-H_2CO	-1.68	-1.58	-0.01	-1.65

Adsorption configurations of possible C-C coupling species

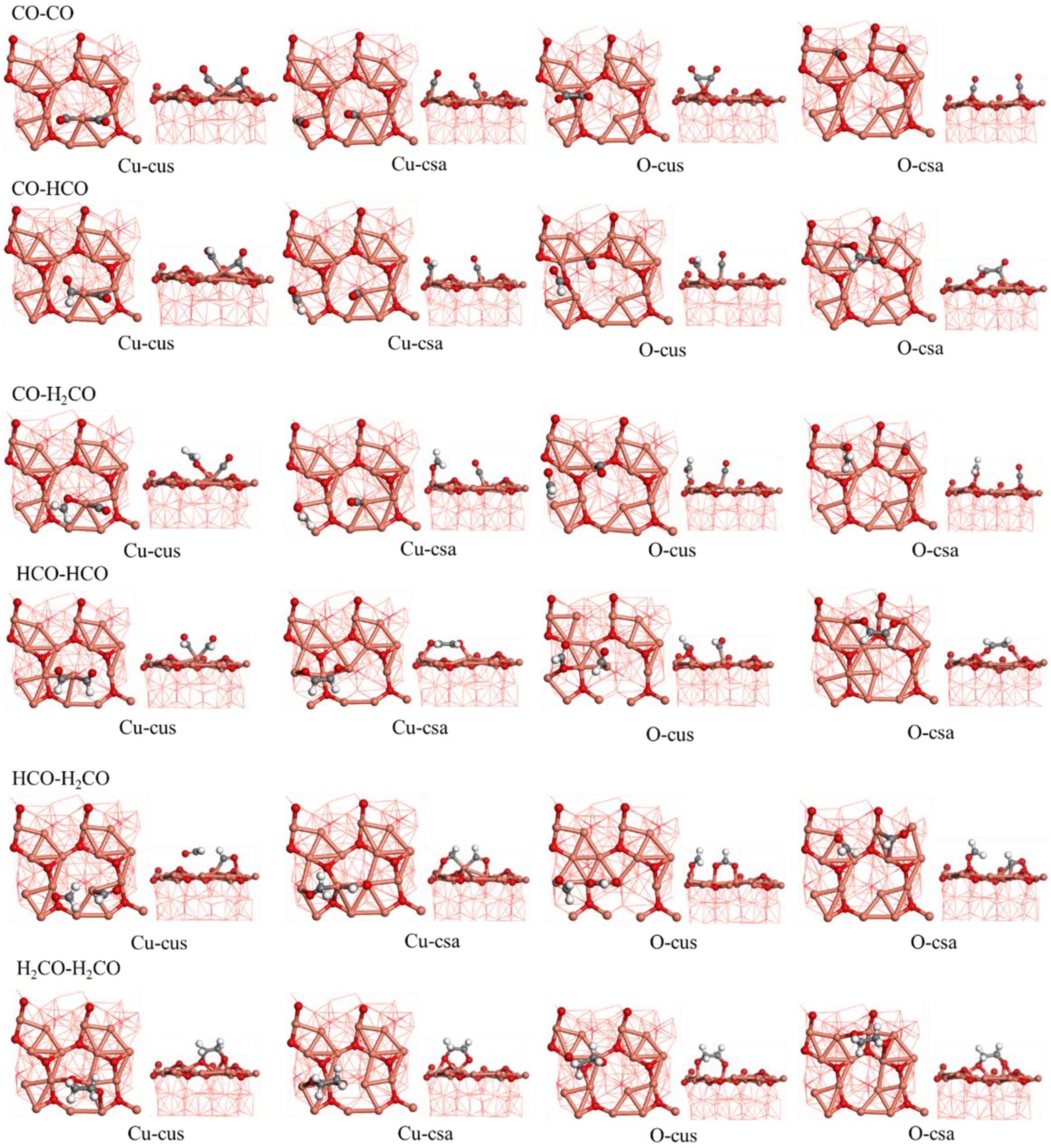

Figure S30 Adsorption configurations of possible C-C coupling species at typical sites over the Cu_2O (111) surface.

Adsorption energy of possible C-C coupling species at different sites with OH pre-adsorbed

In Table S7 the C-C species are co-adsorbed at their most stable site as illustrated in Figure S25, and the OH* are set to adsorb at the Cu_{cus}, Cu_{csa} and $Cu_{neighbor}$ sites, respectively. The stable adsorption configurations are summarized in Figure S26.

Table S8 Adsorption energy (eV) of possible C-C coupling species with OH pre-adsorbed at different sites over the Cu_2O (111) surface.

	Cu_{cus}	Cu_{csa}	$Cu_{neighbor}$
CO-CO	-5.52	-4.84	-5.84
CO-HCO	-5.84	-5.95	-6.03
CO-H_2CO	-4.80	-4.90	-5.07
HCO-HCO	-7.16	-6.87	-7.21
HCO-H_2CO	-4.57	-5.25	-4.76
H_2CO-H_2CO	-4.21	-4.34	-4.43

Adsorption configurations of possible C-C coupling species with OH pre-adsorbed

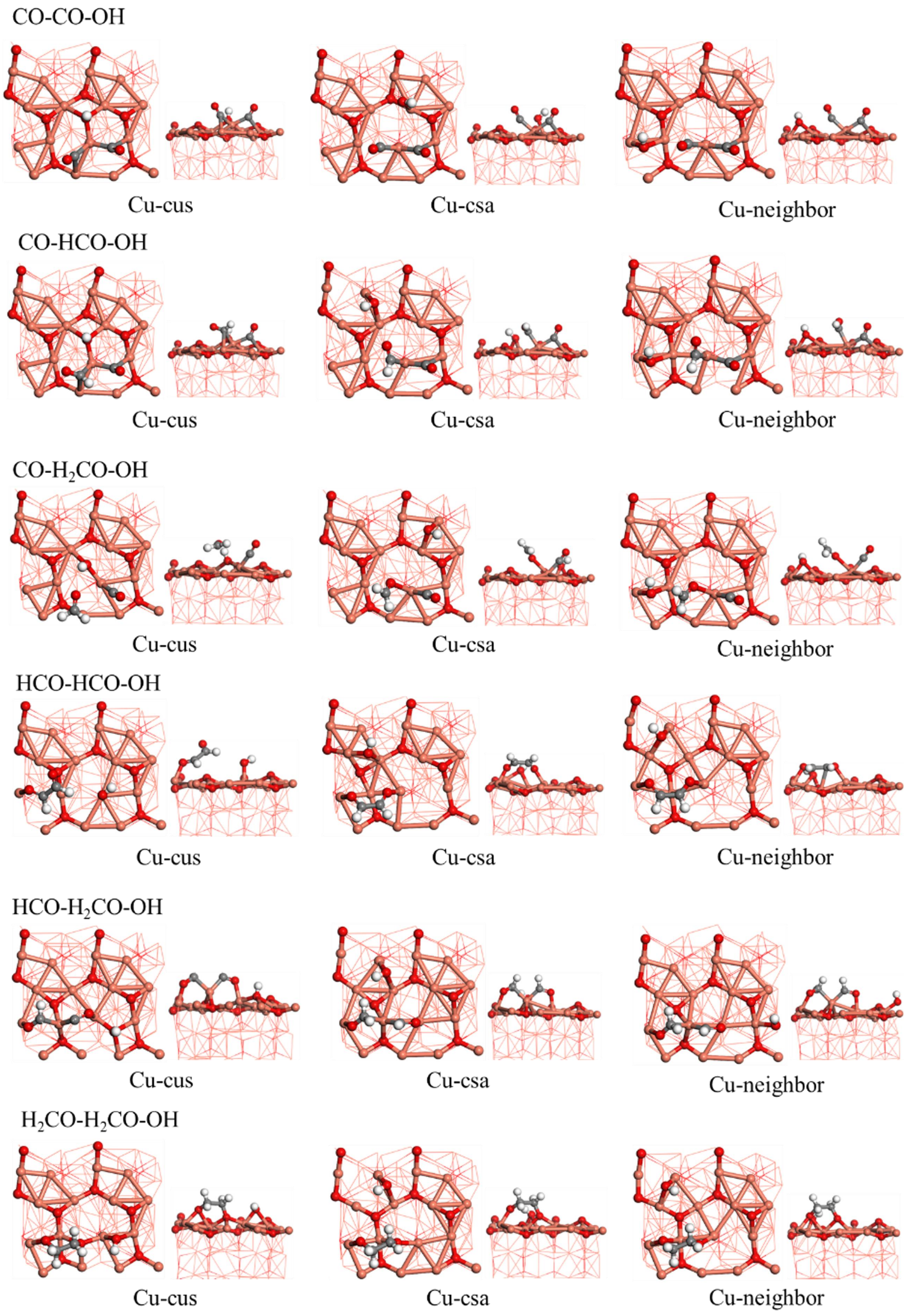

Figure S31 Adsorption configurations of possible C-C coupling species with OH pre-adsorbed at different sites over the Cu_2O (111) surface.

Charge analysis of OH pre-adsorption before and after CO-H_2CO coupling

Table S9 Bader charge of surface Cu, CO-H_2CO and pre-adsorbed OH over Cu_2O surface.

Atom Num	Species kind	CO-H_2CO		OH-CO-H_2CO	
		Before coupling	After coupling	Before coupling	After coupling
1	Cu(left)	10.40	10.67	10.39	10.66
2	Cu(middle)	10.44	10.42	10.45	10.41
3	Cu(right)	10.45	10.37	10.45	10.35
4	C	2.52	2.55	2.62	2.57
5	O	7.71	7.71	7.69	7.71
6	H	0.81	0.87	0.84	0.92
7	H	0.99	0.86	0.86	0.87
8	C	2.24	2.28	2.23	2.28
9	O	7.85	7.85	7.85	7.83
10	O	—	—	7.53	7.52
11	H	—	—	0.00	0.00
Sum of CO-H_2CO		22.11	22.12	22.09	22.19

The atoms are labelled in Figure S31.

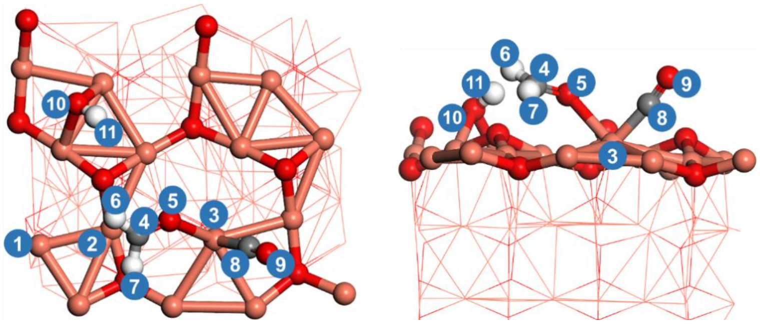

Figure S32 Atomic number of above-mentioned species over Cu_2O surface.

Partial charge distributions of CO-H_2CO before and after coupling

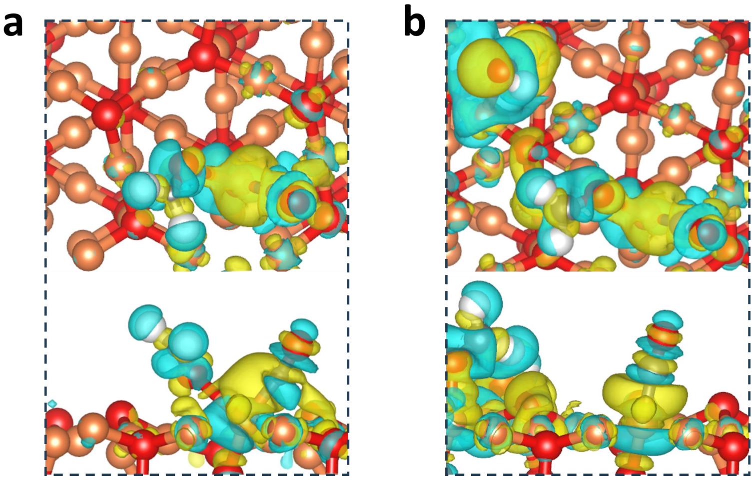

Figure S33 Partial charge distributions of (OH-)CO-H_2CO after coupling (a) CO-H_2CO; (c) OH-CO-H_2CO.

Reaction energy and activation barrier for C2 hydrogenation

Table S10 Reaction energy and activation barrier for C2 hydrogenation.

No.	Elementary step	ΔE (eV)	E_a (eV)
1	$OCCH_2O^* + H^* \rightarrow OCCH_2OH^*$	-0.54	1.27
2	$OCCH_2OH^* + H^* \rightarrow OCCH_2^* + H_2O^*$	0.09	1.10
3	$OCCH_2OH^* \rightarrow OCCH_2^* + OH^*$	0.125	2.75
4	$OCCH_2^* + H^* \rightarrow OHCCH_2^*$	-0.79	1.05
5	$OCCH_2^* + H^* \rightarrow OCCH_3^*$	-1.13	1.41
6	$OHCCHO^* + H^* \rightarrow OHCCHOH^*$	-0.06	0.18
7	$OHCCHOH^* + H^* \rightarrow OHCCH_2OH^*$	-1.27	0.83
8	$OHCCHOH^* \rightarrow OHCCH^* + OH^*$	1.11	3.88
9	$OHCCH_2OH^* \rightarrow OHCCH_2^* + OH^*$	-1.27	1.60
10	$OHCCH_2^* + OH^* + H^* \rightarrow OHCCH_2^* + H_2O^*$	-0.41	0.13
11	$OHCCH_2^* + H^* \rightarrow HOHCCH_2^*$	-0.97	1.40
12	$OHCCH_2^* + H^* \rightarrow OHCCH_3^*$	0.18	1.06
13	$OHCCH_3^* + H^* \rightarrow OH_2CCH_3^*$	-0.59	1.04
14	$OHCCH_3^* + H^* \rightarrow HOHCCH_3^*$	-0.44	1.87
15	$OH_2CCH_3^* + H^* \rightarrow HOH_2CCH_3^*$	-0.78	0.20
16	$HOH_2CCH_3^* \rightarrow HOH_2CCH_3 + {}^*$	1.17	—

Comparison of step hydrogenation

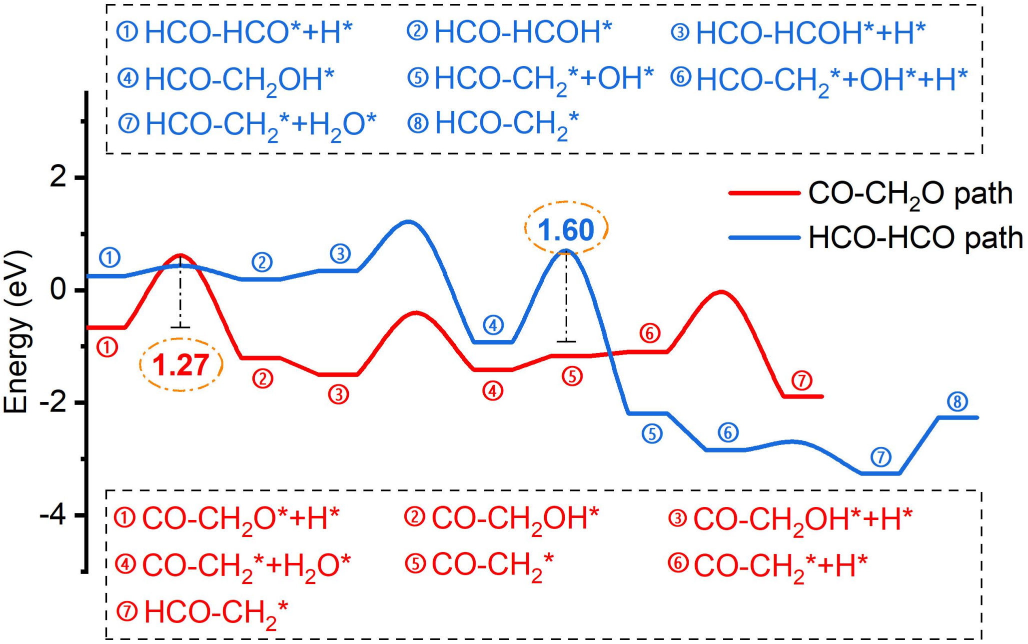

Figure S34 Comparison of step hydrogenation from CO-H$_2$CO* or HCO-HCO* to HCO-CH$_2$*.

The replacement of O in methoxyl and ethoxyl

In Figure S34, the formation reactions of CH_3OH and C_2H_5OH via OH replacement of O show high barriers, which are 1.5 eV and 1.62 eV, respectively. Panel a follows the Langmuir-Hinshelwood mechanism in which OH(g) firstly adsorbs at the neighbor site (saturated Cu_{csa}) and then moves to replace the O to form a C-OH bond. Panel b follows the Eley-Rideal mechanism in which OH(g) moves to directly react with $CH_3CH_2O^*$. The cleavage of C-O in both CH_3OH and C_2H_5OH is very difficult, shown by the rapid increase of the internal energy near the TS steps. In this regard, the formation of an alcohols via OH replacement is quite unfavorable.

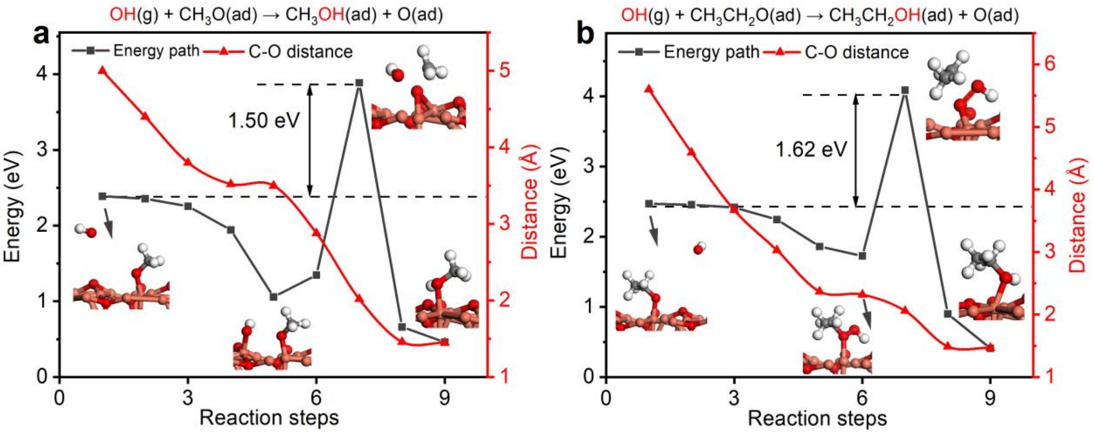

Figure S35 The replacement of O in methoxyl and ethoxyl by gas phase OH to form alcohols via E-R reactions. (a) CH_3OH formation, (b) C_2H_5OH formation.

Adsorption energies and bonding information of C_2H_5OH with H_2O or OH*

Table S11 Adsorption energies and bonding information of C_2H_5OH with H_2O or OH* over the Cu_2O (111) surface.

Co-adsorption species	H_2O/OH adsorption site	C_2H_5OH adsorption site	Total adsorption energy (eV)	C_2H_5OH adsorption energy (eV)
None	—	Cu_{cus}	—	-1.17
H_2O	Cu_{cus}	Unbonded	-2.05	-0.77
H_2O	Unbonded	Cu_{cus}	-2.02	-1.13
OH	Cu_{cus}	Cu_{csa}	-3.79	-0.91
OH	Neighbor Cu_{cus}	Cu_{cus}	-4.06	-1.13

Adsorption configuration of C_2H_5OH

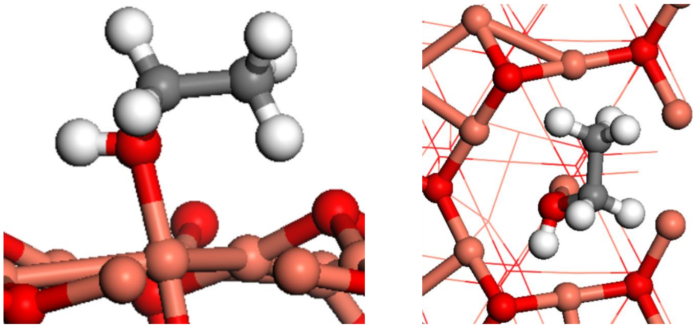

Figure S36 Adsorption configuration of C_2H_5OH over the Cu_2O (111) surface.

The co-adsorption configurations of C_2H_5OH with H_2O or OH

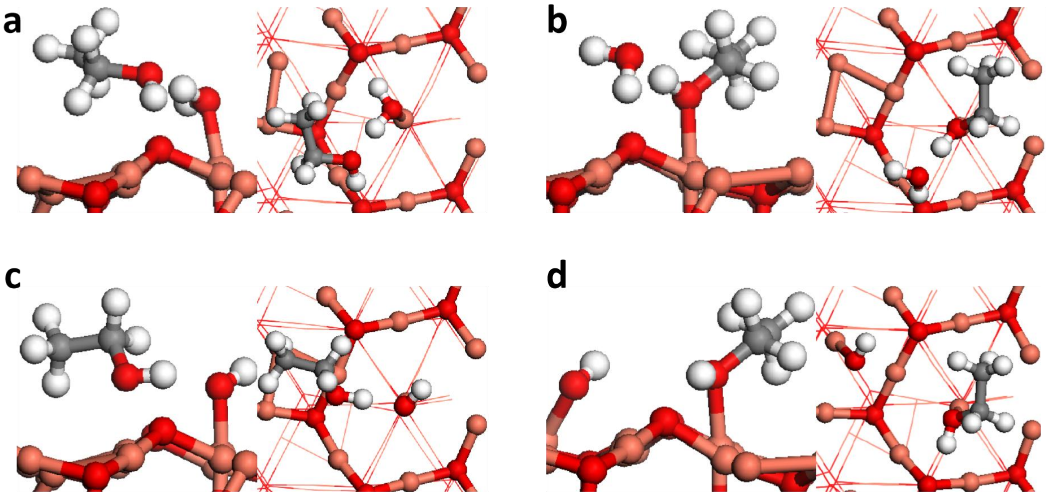

Figure S37 Co-adsorption configurations of C_2H_5OH with H_2O or OH over the Cu_2O (111) surface: (a) H_2O at Cu_{cus} site and C_2H_5OH unbonded; (b) C_2H_5OH at Cu_{cus} site and H_2O unbonded; (c) OH at Cu_{cus} site and C_2H_5OH unbonded; (d) C_2H_5OH at Cu_{cus} site and OH at neighboring Cu_{cus}.

References

(1) Inoue, T.; Iizuka, T.; Tanabe, K., Hydrogenation of carbon-dioxide and carbon-monoxide over supported rhodium catalysts under 10 bar pressure. *Appl. Catal.* **1989**, *46*, 1-9.
(2) Kusama, H.; Okabe, K.; Sayama, K.; Arakawa, H., CO_2 hydrogenation to ethanol over promoted Rh/SiO_2 catalysts. *Catal. Today* **1996**, *28*, 261-266.
(3) Kusama, H.; Okabe, K.; Sayama, K.; Arakawa, H., Ethanol synthesis by catalytic hydrogenation of CO_2 over $Rh\text{-}Fe/SiO_2$ catalysts. *Energy* **1997**, *22*, 343-348.
(4) Yang, C.; Mu, R.; Wang, G.; Song, J.; Tian, H.; Zhao, Z.-J.; Gong, J., Hydroxyl-mediated ethanol selectivity of CO_2 hydrogenation. *Chem. Sci.* **2019**, *10*, 3161-3167.
(5) Goryachev, A.; Pustovarenko, A.; Shterk, G.; Alhajri, N. S.; Jamal, A.; Albuali, M.; van Koppen, L.; Khan, I. S.; Russkikh, A.; Ramirez, A.; Shoinkhorova, T.; Hensen, E. J. M.; Gascon, J., A Multi-Parametric Catalyst Screening for CO_2 Hydrogenation to Ethanol. *Chemcatchem* **2021**, *13*, 3324-3332.
(6) Zhang, F.; Zhou, W.; Xiong, X.; Wang, Y.; Cheng, K.; Kang, J.; Zhang, Q.; Wang, Y., Selective Hydrogenation of CO_2 to Ethanol over Sodium-Modified Rhodium Nanoparticles Embedded in Zeolite Silicalite-1. *J. Phys. Chem. C* **2021**, *125*, 24429-24439.
(7) Bando, K. K.; Soga, K.; Kunimori, K.; Arakawa, H., Effect of Li additive on CO_2 hydrogenation reactivity of zeolite supported Rh catalysts. *Appl. Catal. A* **1998**, *175*, 67-81.
(8) Wang, G.; Luo, R.; Yang, C.; Song, J.; Xiong, C.; Tian, H.; Zhao, Z.-J.; Mu, R.; Gong, J., Active sites in CO_2 hydrogenation over confined VO_x-Rh catalysts. *Sci. China Chem*. **2019**, *62*, 1710-1719.
(9) Zhang, S.; Liu, X.; Shao, Z.; Wang, H.; Sun, Y., Direct CO_2 hydrogenation to ethanol over supported Co_2C catalysts: Studies on support effects and mechanism. *J. Catal.* **2020**, *382*, 86-96.
(10) Zhang, S.; Wu, Z.; Liu, X.; Shao, Z.; Xia, L.; Zhong, L.; Wang, H.; Sun, Y., Tuning the interaction between Na and Co_2C to promote selective CO_2 hydrogenation to ethanol. *Appl. Catal., B* **2021**, *293*, 120207.
(11) Nieskens, D. L. S.; Ferrari, D.; Liu, Y.; Kolonko, R., Jr., The conversion of carbon dioxide and hydrogen into methanol and higher alcohols. *Catal. Commun.* **2011**, *14*, 111-113.
(12) Gnanamani, M. K.; Jacobs, G.; Keogh, R. A.; Shafer, W. D.; Sparks, D. E.; Hopps, S. D.; Thomas, G. A.; Davis, B. H., Fischer-Tropsch synthesis: Effect of pretreatment conditions of cobalt on activity and selectivity for hydrogenation of carbon dioxide. *Appl. Catal. A* **2015**, *499*, 39-46.
(13) Wang, Y.; Wang, K.; Zhang, B.; Peng, X.; Gao, X.; Yang, G.; Hu, H.; Wu, M.; Tsubaki, N., Direct Conversion of CO_2 to Ethanol Boosted by Intimacy-Sensitive Multifunctional Catalysts. *ACS Catal.* **2021**, *11*, 11742-11753.
(14) Lu, F.; Chen, X.; Wang, W.; Zhang, Y., Adjusting the CO_2 hydrogenation pathway via the synergic effects of iron carbides and iron oxides. *Catal. Sci. Technol.* **2021**, *11*, 7694-7703.
(15) Kishida, M.; Yamada, K.; Nagata, H.; Wakabayashi, K., CO_2 hydrogenation for C_{2+} alcohols synthesis over silica-supported Ir-Mo catalysts. *Chem. Lett.* **1994**, 555-556.
(16) Yang, C.; Liu, S.; Wang, Y.; Song, J.; Wang, G.; Wang, S.; Zhao, Z.-J.; Mu, R.; Gong, J., The Interplay between Structure and Product Selectivity of CO_2 Hydrogenation. *Angew. Chem. Int. Ed.* **2019**, *58*, 11242-11247.
(17) Ye, X.; Ma, J.; Yu, W.; Pan, X.; Yang, C.; Wang, C.; Liu, Q.; Huang, Y., Construction of bifunctional single-atom catalysts on the optimized $\beta\text{-}Mo_2C$ surface for highly selective hydrogenation of CO_2 into ethanol. *J. Energy Chem.* **2022**, *67*, 184-192.
(18) He, Z.; Qian, Q.; Ma, J.; Meng, Q.; Zhou, H.; Song, J.; Liu, Z.; Han, B., Water-Enhanced Synthesis of Higher Alcohols from CO_2 Hydrogenation over a Pt/Co_3O_4 Catalyst under Milder Conditions. *Angew. Chem. Int. Ed.* **2016**, *55*, 737-741.
(19) Qian, Q.; Cui, M.; He, Z.; Wu, C.; Zhu, Q.; Zhang, Z.; Ma, J.; Yang, G.; Zhang, J.; Han, B., Highly selective hydrogenation of CO_2 into C_{2+} alcohols by homogeneous catalysis. *Chem. Sci.* **2015**, *6*, 5685-5689.
(20) Liu, S.; Yang, C.; Zha, S.; Sharapa, D.; Studt, F.; Zhao, Z.-J.; Gong, J., Moderate Surface Segregation Promotes Selective Ethanol Production in CO_2 Hydrogenation Reaction over CoCu Catalysts. *Angew. Chem. Int. Ed.* **2022**, *61*, e202109027.
(21) Wang, L.; He, S.; Wang, L.; Lei, Y.; Meng, X.; Xiao, F.-S., Cobalt-Nickel Catalysts for Selective

Hydrogenation of Carbon Dioxide into Ethanol. *ACS Catal.* **2019**, *9*, 11335-11340.

(22) Wang, L.; Wang, L.; Zhang, J.; Liu, X.; Wang, H.; Zhang, W.; Yang, Q.; Ma, J.; Dong, X.; Yoo, S. J.; Kim, J.-G.; Meng, X.; Xiao, F.-S., Selective Hydrogenation of CO_2 to Ethanol over Cobalt Catalysts. *Angew. Chem. Int. Ed.* **2018**, *57*, 6104-6108.

(23) Wang, D.; Bi, Q.; Yin, G.; Zhao, W.; Huang, F.; Xie, X.; Jiang, M., Direct synthesis of ethanol via CO_2 hydrogenation using supported gold catalysts. *Commun. Chem.* **2016**, *52*, 14226-14229.

(24) Zhang, H.; Han, H.; Xiao, L.; Wu, W., Highly Selective Synthesis of Ethanol via CO_2 Hydrogenation over $CoMoC_x$ Catalysts. *ChemCatChem* **2021**, *13*, 3333-3339.

(25) Ye, X.; Yang, C.; Pan, X.; Ma, J.; Zhang, Y.; Ren, Y.; Liu, X.; Li, L.; Huang, Y., Highly Selective Hydrogenation of CO_2 to Ethanol via Designed Bifunctional Ir_1-In_2O_3 Single-Atom Catalyst. *J. Am. Chem. Soc.* **2020**, *142*, 19001-19005.

(26) Lou, Y.; Jiang, F.; Zhu, W.; Wang, L.; Yao, T.; Wang, S.; Yang, B.; Yang, B.; Zhu, Y.; Liu, X., CeO_2 supported Pd dimers boosting CO_2 hydrogenation to ethanol. *Appl. Catal., B* **2021**, *291*, 120122.

(27) An, B.; Li, Z.; Song, Y.; Zhang, J.; Zeng, L.; Wang, C.; Lin, W., Cooperative copper centres in a metal-organic framework for selective conversion of CO_2 to ethanol. *Nat. Catal.* **2019**, *2*, 709-717.

(28) Zhao, K.; Liu, Y.; Quan, X.; Chen, S.; Yu, H., CO_2 Electroreduction at Low Overpotential on Oxide-Derived Cu/Carbons Fabricated from Metal Organic Framework. *ACS Appl. Mater. Interfaces* **2017**, *9*, 5302-5311.

(29) Zhu, Q.; Sun, X.; Yang, D.; Ma, J.; Kang, X.; Zheng, L.; Zhang, J.; Wu, Z.; Han, B., Carbon dioxide electroreduction to C_2 products over copper-cuprous oxide derived from electrosynthesized copper complex. *Nat. Commun.* **2019**, *10*, 3851.

(30) Lee, S.; Park, G.; Lee, J., Importance of Ag-Cu Biphasic Boundaries for Selective Electrochemical Reduction of CO_2 to Ethanol. *ACS Catal.* **2017**, *7*, 8594-8604.

(31) Ren, D.; Ang, B. S.-H.; Yeo, B. S., Tuning the Selectivity of Carbon Dioxide Electroreduction toward Ethanol on Oxide-Derived Cu_xZn Catalysts. *ACS Catal.* **2016**, *6*, 8239-8247.

(32) Zhu, W.; Zhao, K.; Liu, S.; Liu, M.; Peng, F.; An, P.; Qin, B.; Zhou, H.; Li, H.; He, Z., Low-overpotential selective reduction of CO_2 to ethanol on electrodeposited Cu_xAu_y nanowire arrays. *J. Energy Chem.* **2019**, *37*, 176-182.

(33) Song, Y.; Peng, R.; Hensley, D. K.; Bonnesen, P. V.; Liang, L.; Wu, Z.; Meyer, H. M., III; Chi, M.; Ma, C.; Sumpter, B. G.; Rondinone, A. J., High-Selectivity Electrochemical Conversion of CO_2 to Ethanol using a Copper Nanoparticle/N-Doped Graphene Electrode. *ChemistrySelect* **2016**, *1*, 6055-6061.

(34) Yuan, J.; Yang, M.-P.; Zhi, W.-Y.; Wang, H.; Wang, H.; Lu, J.-X., Efficient electrochemical reduction of CO_2 to ethanol on Cu nanoparticles decorated on N-doped graphene oxide catalysts. *J. CO_2 Util.* **2019**, *33*, 452-460.

(35) Xu, H.; Rebollar, D.; He, H.; Chong, L.; Liu, Y.; Liu, C.; Sun, C.-J.; Li, T.; Muntean, J. V.; Winans, R. E.; Liu, D.-J.; Xu, T., Highly selective electrocatalytic CO_2 reduction to ethanol by metallic clusters dynamically formed from atomically dispersed copper. *Nat. Energy* **2020**, *5*, 623-632.

(36) Li, F.; Li, Y. C.; Wang, Z.; Li, J.; Nam, D.-H.; Lum, Y.; Luo, M.; Wang, X.; Ozden, A.; Hung, S.-F.; Chen, B.; Wang, Y.; Wicks, J.; Xu, Y.; Li, Y.; Gabardo, C. M.; Dinh, C.-T.; Wang, Y.; Zhuang, T.-T.; Sinton, D.; Sargent, E. H., Cooperative CO_2-to-ethanol conversion via enriched intermediates at molecule-metal catalyst interfaces. *Nat. Catal*. **2020**, *3*, 75-82.

(37) Liu, Y.; Fan, X.; Nayak, A.; Wang, Y.; Shan, B.; Quan, X.; Meyer, T. J., Steering CO_2 electroreduction toward ethanol production by a surface-bound Ru polypyridyl carbene catalyst on N-doped porous carbon. *Proc. Natl. Acad. Sci.* **2019**, *116*, 26353-26358.